An Investigation of Sound Radiation by Supersonic Unstable Modes in Hypersonic Boundary Layers

Carleton P. Knisely* and Xiaolin Zhong†

University of California, Los Angeles, California, 90095, USA

There has been a renewed interest in studying hypersonic boundary layer stability in flows with highly-cooled walls due to its applicability to experiments and some real flight conditions. One physical phenomenon that occurs in these flows is the creation of a supersonic mode, also referred to as the spontaneous radiation of sound. The spontaneous radiation of sound is associated with an unstable Mack's second mode synchronizing with the slow acoustic spectrum, causing the disturbance to travel upstream supersonically relative to the meanflow outside the boundary layer. Previous studies have focused specifically on a two-dimensional flat plate geometry and have assumed chemical equilibrium, or have focused on a sharp cone geometry. However, the spontaneous radiation of sound is yet to be investigated in detail on an axisymmetric blunt cone. This study aims to investigate the existence of the spontaneous radiation of sound in Mach 5 flow over a 1 mm nose radius cold-wall cone using thermochemical nonequilibrium LST and DNS studies and investigate in further detail the impact of supersonic modes on disturbance growth. Results indicate that the supersonic mode creates an abnormal growth pattern that is not observed in traditional flows with second-mode transition. This behavior could have an impact on energy transfer and boundary layer stability.

I. Introduction

It has long been known that boundary layer transition from laminar to turbulent has a considerable impact on the design of hypersonic vehicles. Transition to turbulent flow drastically increases drag and heating to the vehicle surface, and can have a prominent effect on control of the hypersonic vehicle. It also affects engine performance and operability as well as vehicle structure and weight. The heating to the vehicle surface is one of the primary considerations in hypersonic vehicle design. Thermal protection systems (TPSs) are required to prevent the surface of the vehicle from overheating and failing. TPSs are usually specified with a large factor of safety to ensure protection of the vehicle, although this often adds unnecessary weight, reducing the maximum payload. The ability to predict accurately or even to delay the onset of transition and maintain laminar flow can have a significant payoff in terms of the reduction in aerodynamic heating, higher fuel efficiency, and weight of the thermal protection system.

Mack[1] found that the major instability waves leading to transition to turbulence in a perfect gas flow are the first and second modes, which Fedorov[2] recently described as acoustic rays physically trapped between the wall and sonic line. Researchers have subsequently developed numerical tools to predict transition to turbulence due to the first and second mode. Malik[3] implemented multiple numerical methods for solving the Linear Stability Theory (LST) equations for a perfect gas. Chemical nonequilibrium effects in the LST framework were studied numerically by Stuckert and Reed.[4] Hudson et al.[5] incorporated thermal nonequilibrium effects in addition to chemical nonequilibrium for LST. Johnson et al.[6–8] studied hypersonic boundary layer transition in thermochemical nonequilibrium using the Parabolized Stability Equations (PSE), which account for nonparallel flow effects that are ignored in LST. Overall, the researchers determined that dissociation of air species is stabilizing to the first mode, but destabilizing to the second mode. Additionally, it was determined that thermal nonequilibrium has a slight destabilizing effect on the first mode, and a slight

*Graduate Student, Mechanical and Aerospace Engineering, carleton.knisely@gmail.com, AIAA Student Member.

†Professor, Mechanical and Aerospace Engineering, xiaolin@seas.ucla.edu, AIAA Associate Fellow.

stabilizing effect on the second mode. These contemporary studies have primarily focused on flows with relatively modest levels of wall cooling with the wall-to-edge temperature ratio greater than unity. ($T_w/T_e > 1$). This motivated Bitter and Shepherd[9] to examine the effect of highly cooled walls on hypersonic boundary layer stability.

Flows with highly cooled walls are of interest in high-enthalpy flows, such as shock tube experiments in which the wall temperature remains ambient during the short test duration, as well as some real flight cases.[10,11] It has long been known through studies by Lees[12] and Mack[13,14] that wall cooling stabilizes the first mode but destabilizes the second mode. Bitter and Shepherd[9] took these studies a few steps further and have recently shown through a chemical equilibrium, thermal nonequilibrium LST analysis that high levels of wall cooling on a flat plate lead to unique features, in particular an unstable second mode traveling upstream supersonically relative to the free stream. The supersonic modes cause second-mode instabilities over a wider range of frequencies than subsonic modes. The unstable supersonic modes cause acoustic waves to radiate from the wall into the free stream. This phenomenon has been referred to as the spontaneous radiation of sound.[15] Figure 1, adapted from Bitter and Shepherd,[9] compares contours of temperature fluctuations at two different frequencies. Note that the perturbations are confined to within the boundary layer for the subsonic mode, but extend well into the free stream for the supersonic mode.

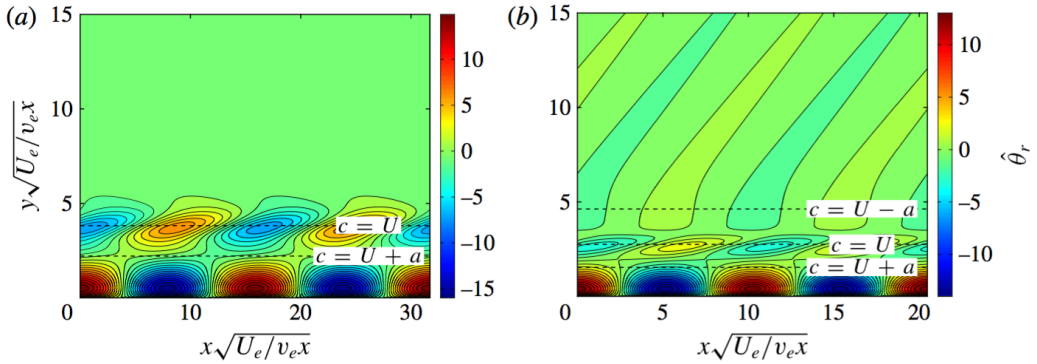

Figure 1: Contours of temperature fluctuations. Adapted from Bitter and Shepherd.[9] $R = 2000$, $T_e = 1500K$, $T_w = 300K$, $Ma = 5$: (a) $\Omega = 0.35$, subsonic mode. (b) $\Omega = 0.45$, supersonic mode.

A schematic of the supersonic mode is presented in Figure 2 for further elaboration. A useful parameter describing the speed of propagation of the disturbance relative to the mean flow is the relative Mach number

$$M_r = \frac{\overline{u} - c_r}{\overline{a}} \tag{1}$$

where $\overline{u}$ is the mean flow velocity tangential to the wall, $c_r = \omega/\sqrt{\beta^2 + \alpha_r^2}$ is the disturbance propagation speed, and $\overline{a}$ is the mean flow speed of sound. Near the wall, $\overline{u}$ is small and the disturbance is traveling supersonically downstream relative to the mean flow, indicated below a relative Mach number of $M_r < -1$. The sonic line $M_r = -1$ acts as a wave guide for the acoustic rays,[2] resulting in the traditional Mack modes. Outside of $M_r = -1$, the disturbance is traveling subsonically with respect to the freestream, and creates a "rope-like" wave pattern observed by many researchers both experimentally[16,17] and numerically.[18–20] In some flows in which the wall temperature is significantly less than the freestream temperature, a second supersonic region can be present. Outside of $M_r = 1$, the disturbance is traveling upstream supersonically with respect to the freestream. This creates the "slanted" wave pattern outside of the boundary layer shown in Figure 1(b). The angle created by this wave pattern is analogous to a Mach wave angle from traditional compressible flow theory, and is given by $\mu = \arcsin(1/M_r)$.

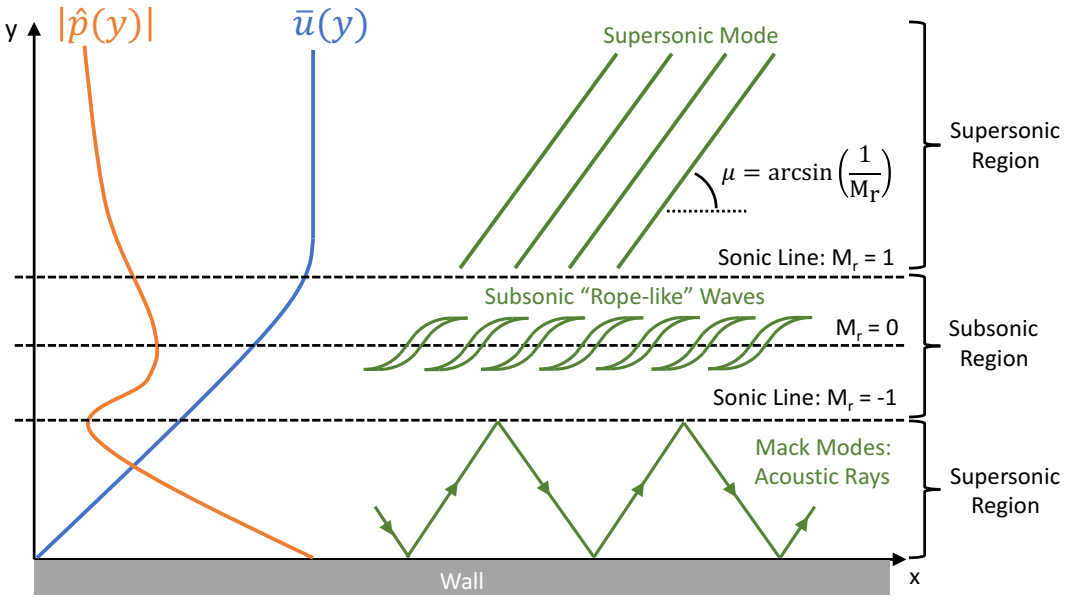

Figure 2: Schematic of supersonic mode.

Chuvakhov and Fedorov[15] confirmed Bitter and Shepherd's[9] findings through LST analysis as well as unsteady direct numerical simulation (DNS) analysis. Supersonic modes are not a new finding, however, and have in fact been identified in a number of other flow configurations. Mack[13] commented on neutral supersonic waves in flow over a flat plate. Chang, Vinh, and Malik[21] reported supersonic modes in Mach 20 flow over a 6 degree wedge with wall temperature ratio $T_w/T_{ad} = 0.1$. Fedorov, Soudakov, and Leyva[22] found unstable supersonic modes in flow with gas injection. Fedorov et al.[23] encountered unstable supersonic modes in flow with resonating micro-cavities. Bres et al.[24] also found this phenomenon in flow over a wall with a porous coating. Wagnild[25] observed the spontaneous radiation of sound, although the focus of his study was the effect of vibrational nonequilibrium. Salemi et al. modeled configurations typical of the T5 tunnel at Caltech and investigates second mode synchronization with the slow acoustic spectrum. They investigated the effect of nonlinear disturbances,[26,27] a flared cone geometry,[28] and high-temperature effects,[29] although the Prandtl number and ratio of specific heats were fixed in their real gas model.

Despite the evidence presented by Bitter and Shepherd[9] and Chuvakhov and Fedorov,[15] it is possible that the impact of the highly-cooled wall on the spontaneous radiation of sound may have been overstated because chemical nonequilibrium was not accounted for. Recent theoretical results by Anatoli Tumin[30] indicate the spontaneous radiation of sound in flows with $T_w/T_e > 1$. This phenomenon may be attributed to the real gas effect and may have been overlooked in previous simulations assuming chemical equilibrium. This study aims to confirm the spontaneous radiation of sound in hypersonic flow over a cold-wall blunt cone using thermochemical nonequilibrium LST and DNS studies. The goal is to verify that the techniques used here are appropriate in studying supersonic modes and can be used in future studies of the spontaneous radiation of sound in flows with $T_w/T_e > 1$.

II. Simulation Conditions

The flow conditions for this study are summarized in Table 1. The geometry is a 5 degree half-angle axisymmetric blunt cone 1 meter in length with a nose radius of 1 mm. The DNS simulation used 256 points in the wall-normal direction and roughly 10 points per millimeter on the surface of the cone in the streamwise direction. In the azimuthal direction, four points are used. LST simulations interpolated the DNS meanflow onto the LST grid defined by the stretching methods discussed in the following sections.

Table 1: Flow conditions for DNS simulations.

Parameter	Value
M_∞	5
$H_{0,\infty}$	9.17 MJ/kg
ρ_∞	2.322 E-2 kg/m^3
p_∞	10 kPa
T_w	300 K
T_w/T_∞	0.2

As will be explained in the following sections, the DNS code used in this study utilizes a shock-fitting method. Thus, the parameters in Table 1 are the free stream conditions upstream of the shock formed over the body. The flow conditions for this study are intended to be similar to those used by Bitter and Shepherd.[9] The overall goal of this study was to confirm the DNS and LST methods were capable of producing the same physical artifacts on a blunt cone observed by Bitter and Shepherd[9] on a flat plate.

III. Governing Equations and Gas Model

The governing equations for the DNS and LST codes are those developed by Mortensen and Zhong,[31–36] which are formulated for thermochemical nonequilibrium assuming a two-temperature model. Their formulation is presented here for clarity. The rotational mode is assumed to be fully excited with up to eleven non-ionizing species with finite-rate chemistry. Two-temperatures are used to represent translation-rotation energy and vibration energy. There are two species models: an eleven-species model (N_2, O_2, NO, C_3, CO_2, C_2, CO, CN, N, O, C) used for ablation studies and a five-species model (N_2, O_2, NO, N, and O) used to simulate air. The five species model is used here. The Navier-Stokes equations in conservative form consist of five species mass conservation equations, three momentum conservation equations, the total energy equation, and the vibration energy equation. The governing equations in vector form are written as

$$\frac{\partial U}{\partial t} + \frac{\partial F_j}{\partial x_j} + \frac{\partial G_j}{\partial x_j} = W \tag{2}$$

where U is the state vector of conserved quantities and W is the source terms defined by

$$U = \begin{bmatrix} \rho_1 \\ \vdots \\ \rho_{ns} \\ \rho u_1 \\ \rho u_2 \\ \rho u_3 \\ \rho e \\ \rho e_v \end{bmatrix}, \quad W = \begin{bmatrix} \omega_1 \\ \vdots \\ \omega_{ns} \\ 0 \\ 0 \\ 0 \\ 0 \\ \sum_{s=1}^{nms} \left(Q_{T-V,s} + \omega_s e_{v,s} \right) \end{bmatrix}.$$

The inviscid and viscous flux vectors, F_j and G_j, respectively, are defined by

$$F_j = \begin{bmatrix} \rho_1 u_j \\ \vdots \\ \rho_{ns} u_j \\ \rho u_1 u_j + p\delta_{1j} \\ \rho u_2 u_j + p\delta_{2j} \\ \rho u_3 u_j + p\delta_{3j} \\ (p + \rho e)\, u_j \\ \rho e_v u_j \end{bmatrix}, \quad G_j = \begin{bmatrix} \rho_1 v_{1j} \\ \vdots \\ \rho_{ns} v_{nsj} \\ \tau_{1j} \\ \tau_{2j} \\ \tau_{3j} \\ -u_i \tau_{ij} - k_T \frac{\partial T}{\partial x_j} - k_V \frac{\partial T_V}{\partial x_j} + \sum_{s=1}^{nms} \rho_s h_s v_{sj} \\ -k_V \frac{\partial T_V}{\partial x_j} + \sum_{s=1}^{nms} \rho_s e_{v,s} v_{sj} \end{bmatrix}.$$

where v_{sj} is the species diffusion velocity, and

$$\tau_{ij} = \mu\left(\frac{\partial u_i}{\partial x_j} + \frac{\partial u_j}{\partial x_i}\right) - \frac{2}{3}\mu\frac{\partial u_k}{\partial x_k}\delta_{ij} \tag{3}$$

is the viscous stress. The total energy per unit volume, ρe, is defined as

$$\rho e = \sum_{s=1}^{ns} \rho_s c_{v,s} T + \rho e_v + \frac{1}{2}\rho\left(u_1^2 + u_2^2 + u_3^2\right) + \sum_{s=1}^{ns} \rho_s h_s^o \tag{4}$$

where h_s^o is the species heat of formation, $e_{v,s}$ is the species specific vibration energy, and $c_{v,s}$ is the species translation-rotation specific heat at constant volume, defined as

$$c_{v,s} = \begin{cases} \frac{5}{2}\frac{\mathcal{R}}{M_s} & s = 1, 2, \ldots, nms \\ \frac{3}{2}\frac{\mathcal{R}}{M_s} & s = nms+1, \ldots, ns. \end{cases} \tag{5}$$

The vibration energy per unit volume, ρe_v, is defined as

$$\rho e_v = \sum_{s=1}^{nms} \rho_s e_{v,s} = \sum_{s=1}^{nms} \rho_s \frac{\mathcal{R}}{M_s}\frac{\theta_{v,s}}{\exp\left(\theta_{v,s}/T_V\right) - 1} \tag{6}$$

where $\theta_{v,s}$ denotes the characteristic vibrational temperature of each vibrational mode. The characteristic vibration temperatures are taken from Park.[37]

To model chemical nonequilibrium, three dissociation reactions and three exchange reactions are used. Each reaction is governed by a forward and backward reaction rate determined from

$$k_f = C_f T_a^{\eta} \exp\left(-\theta_d/T_a\right) \tag{7}$$

$$k_b = k_f/K_{eq} \tag{8}$$

where all forward reaction rates are obtained from Park.[37] The equilibrium coefficient, K_{eq}, is determined using

$$K_{eq} = A_0 \exp\left(\frac{A_1}{Z} + A_2 + A_3\ln(Z) + A_4 Z + A_5 Z^2\right), \quad Z = \frac{10000}{T} \tag{9}$$

which is a curve fit to experimental data from Park.[37]

The Landau-Teller formulation is used to calculate the source term in the vibration energy equation representing the exchange of energy between the translation-rotation and vibration energies

$$Q_{T-V,s} = \rho_s \frac{e_{v,s}(T) - e_{v,s}(T_V)}{<\tau_s> + \tau_{cs}} \tag{10}$$

where $<\tau_s>$ is the Landau-Teller relaxation time given by Lee.[38] The term τ_{cs} is from Park[37] to more accurately model the relaxation time in areas of high temperatures occurring just downstream of the bow shock.

The viscosity of each species is computed using a Blottner curve fit shown in Eq. 11. The coefficients are obtained from Blottner et al.[39] The mixture viscosity is then found using each species viscosity from Wilke's[40] mixing rule (Eq. 12). The total heat conductivities for each energy mode are computed in a similar fashion as viscosity. The diffusion velocity is calculated using Fick's law and a constant Schmidt number of 0.5.

$$\mu_s = 0.1\exp\left[\left(A_s^{\mu}\ln(T) + B_s^{\mu}\right)\ln(T) + C_s^{\mu}\right] \tag{11}$$

$$\mu = \sum_{s=1}^{ns} \frac{X_s \mu_s}{\phi_s} \tag{12}$$

IV. Numerical Methods

A. DNS

The thermochemical nonequilibrium code developed by Mortensen and Zhong[31–36] utilizes a high-order shock-fitting method extended from a perfect gas flow version by Zhong[41] to compute the flow field between the shock and the body. The numerical method is repeated here for clarity. For shock-fitting computations the shock location is not known *a priori*, so its position is solved along with the flow field. Since the shock position is not stationary, the grid used to compute the flow field is a function of time. This leads to the coordinate transformation

$$\begin{cases} \xi = \xi(x,y,z) \\ \eta = \eta(x,y,z,t) \\ \zeta = \zeta(x,y,z) \\ \tau = t \end{cases} \iff \begin{cases} x = x(\xi,\eta,\zeta,\tau) \\ y = y(\xi,\eta,\zeta,\tau) \\ z = z(\xi,\eta,\zeta,\tau) \\ t = \tau \end{cases} \tag{13}$$

where y is normal to the body, x is in the streamwise direction, z is in the transverse direction, $\zeta_t = 0$, and $\xi_t = 0$. The governing equation can then be transformed into computational space as

$$\frac{1}{J}\frac{\partial U}{\partial \tau} + \frac{\partial E'}{\partial \xi} + \frac{\partial F'}{\partial \eta} + + \frac{\partial G'}{\partial \zeta} + \frac{\partial E'_v}{\partial \xi} + \frac{\partial F'_v}{\partial \eta} + + \frac{\partial G'_v}{\partial \zeta} + U\frac{\partial (1/J)}{\partial \tau} = \frac{W}{J} \tag{14}$$

where J is the Jacobian of the coordinate transformation and

$$E' = \frac{F_1\xi_x + F_2\xi_y + F_3\xi_z}{J} \tag{15}$$

$$F' = \frac{F_1\eta_x + F_2\eta_y + F_3\eta_z}{J} \tag{16}$$

$$G' = \frac{F_1\zeta_x + F_2\zeta_y + F_3\zeta_z}{J} \tag{17}$$

$$E'_v = \frac{G_1\xi_x + G_2\xi_y + G_3\xi_z}{J} \tag{18}$$

$$F'_v = \frac{G_1\eta_x + G_2\eta_y + G_3\eta_z}{J} \tag{19}$$

$$G'_v = \frac{G_1\zeta_x + G_2\zeta_y + G_3\zeta_z}{J}. \tag{20}$$

A seven point stencil is used to discretize the spatial derivatives

$$\frac{\partial f_i}{\partial x} = \frac{1}{hb_i}\sum_{k=-3}^{3}\alpha_{i+k}f_{i+k} - \frac{\alpha}{6!b_i}h^5\left(\frac{\partial f^6}{\partial^6 x}\right) \tag{21}$$

where

$$\alpha_{i\pm3} = \pm 1 + \frac{1}{12}\alpha, \qquad \alpha_{i\pm2} = \mp 9 - \frac{1}{2}\alpha$$
$$\alpha_{i\pm1} = \pm 45 + \frac{5}{4}\alpha, \qquad \alpha_i = -\frac{5}{3}\alpha$$
$$b_i = 60$$

and where h is the step size, $\alpha < 0$ is a fifth order upwind explicit scheme, and $\alpha = 0$ reduces to a sixth order central scheme. Here the inviscid terms use $\alpha = -6$ which yields a low dissipation fifth order upwinded difference and the viscous terms are discretized using $\alpha = 0$. The derivatives in the transverse direction, if required, are treated with Fourier collocation. To compute second derivatives, the first order derivative operator is applied twice.

Flux splitting is used for the inviscid flux terms resulting in

$$F' = F'^{+} + F'^{-} \tag{22}$$

where

$$F'^{\pm} = \frac{1}{2}(F' \pm \Lambda U) \tag{23}$$

and Λ is a diagonal matrix that ensures F'^{+} and F'^{-} contain only pure positive and negative eigenvalues, respectively. For thermochemical nonequilibrium, the eigenvalues of Λ were derived by Liu and Vinokur.[42]

Conditions behind the shock are calculated from Rankine-Hugoniot relations. In the freestream, the flow is assumed to be in thermal equilibrium and the chemical composition of the flow is frozen. The shock is assumed to be infinitely thin which means that the flow has no time to relax as it crosses the shock as relaxation rates are finite. This leads to the chemical composition remaining constant across the shock, as well as the vibration temperature. Since neither process has any time to relax across the shock, the relaxation zone is entirely downstream of the shock. A complete derivation of thermochemical nonequilibrium shock fitting can be found in Prakash et al.[43] A low storage 3rd-order Runge-Kutta method from Williamson[44] is used to advance the solution in time.

B. LST

The linear stability analysis used here is largely based on the LST code developed by Mortensen,[36] however here the assumption of zero wall-normal velocity is relaxed (i.e. $\overline{v} \neq 0$), and new freestream boundary conditions incorporating a shock at the computational boundary are used. A body-fitted orthogonal curvilinear coordinate system is used for axisymmetric bodies where x is in the streamwise direction, y is in the wall-normal direction, z is in the transverse direction, and the origin is located on the body surface. Curvature in the streamwise and transverse directions is included similar to Malik and Spall.[45] Elemental lengths are defined as $h_1 dx$, dy, and $h_3 dz$ where

$$h_1 = 1 + \kappa y \tag{24}$$

$$h_3 = r_b + y\cos(\theta) \tag{25}$$

and where κ is the streamwise curvature, r_b is the local radius of the body, and θ is the local half angle of the body. The coordinate system for a flat plate is recovered by setting h_1 and h_3 to unity. For a straight cone, only h_3 is required and h_1 is set to unity.

The derivation of the thermochemical nonequilibrium LST equations follows the work of Hudson.[5,46] The main difference in the derivation is that here the equation for each species velocity is substituted into the governing equations before they are linearized, similar to Klentzman et al.[47] The LST equations are derived from the governing equations (Eq. 2) where the instantaneous flow is comprised of a mean and fluctuating component $q = \overline{q} + q'$. Here q represents any flow variable such as velocity, density, temperature, etc. The instantaneous flow is then substituted into the governing equations where the steady flow is assumed to satisfy the governing equations and is subtracted out. The mean flow is assumed to be a function of y only i.e. $\overline{q}(x, y, z) = \overline{q}(y)$ and the flow disturbances are assumed to be small i.e. linear. The perturbations are then assumed to be in the form of a normal mode described by

$$q' = \hat{q}(y)\exp\left[i\left(\alpha x + \beta z - \omega t\right)\right] \tag{26}$$

where ω is the circular frequency of the disturbance and α and β are the wavenumbers. Commonly ω and β are assumed to be real and the wavenumber α is assumed to be complex which means the disturbances grow in space rather than time. If ω is complex and α and β are real then the disturbances grow in time rather than space. For comparison to direct numerical simulation the spatial stability approach is used i.e. α is complex which results in the dispersion relation $\alpha = \Omega(\omega, \beta)$. Substituting in the normal mode form for the perturbation reduces the problem to a coupled set of $ns + 5$ ordinary differential equations

$$\left(\mathbf{A}\frac{d^2}{dy^2} + \mathbf{B}\frac{d}{dy} + \mathbf{C}\right)\vec{\phi} = \vec{0}. \tag{27}$$

where $\vec{\phi} = \left[\hat{\rho}_1, \hat{\rho}_2, \ldots, \hat{\rho}_{ns}, \hat{u}, \hat{v}, \hat{w}, \hat{T}, \hat{T}_V\right]^T$ and $\mathbf{A}$, $\mathbf{B}$ and $\mathbf{C}$ are complex square matrices of size $ns+5$. This is now a boundary value problem where the derivative operators can be discretized and the equations solved numerically.

For hypersonic compressible boundary layers it is important to have high grid resolution near the generalized inflection point.[1] The grid used by Mortensen[36] uses two different functions to cluster points around

the inflection point and near the wall. It is called the cosine-exponential grid. For some boundary layers, there is a sharp increase in the eigenfunctions near the wall for the temperatures and densities that was not captured correctly with the grid that only clustered points near the inflection point, such as a grid similar to the one used by Hudson et al.[5] Mortensen's[36] cosine-exponential grid was much more effective for boundary layers with strong changes in the eigenfunctions near the wall. The cosine-exponential grid is defined so that

$$y = \begin{cases} y_i \left(1 - \cos(\pi\eta)\right)/2, & 0 \le y \le y_i \\ y_i + \frac{a\eta}{b-\eta}, & y > y_i \end{cases} \tag{28}$$

where

$$a = (y_{max} - y_i)s \tag{29}$$

$$b = \frac{1+a}{y_{max} - y_i} \tag{30}$$

and y_{max} is the outer domain boundary, y_i is the location of the generalized inflection point, η runs from zero to one, and s is a stretching parameter that stretches towards y_i for $s < 1$ and away for $s > 1$. Here, s = 0.5 was used. Grid metrics can be computed directly from Eq. 28.

In hypersonic flows in which the spontaneous radiation of sound occurs, the cosine-exponential grid may not provide enough grid resolution in the free stream or near the outer shock boundary. The continuous modes oscillate to the computational boundary in many cases. Therefore, it is helpful to use an additional exponential grid stretching function at the edge of the computational boundary. The new cosine-double-exponential grid is defined so that

$$y = \begin{cases} y_{i,1} \left(1 - \cos(\pi\eta)\right)/2, & 0 \le y \le y_{i,1} \\ y_{i,1} + \frac{a_1\eta}{b_1-\eta}, & y_{i,1} < y \le y_{i,2} \\ y_{max} - \frac{a_2\eta}{b_2-\eta}, & y > y_{i,2} \end{cases} \tag{31}$$

where

$$a_1 = (y_{i,2} - y_{i,1})s_1, \quad a_2 = (y_{max} - y_{i,2})s_2 \tag{32}$$

$$b_1 = \frac{1+a_1}{y_i, 2 - y_{i,1}}, \quad b_2 = \frac{1+a_2}{y_{max} - y_{i,2}} \tag{33}$$

where similar to the original cosine-exponential grid, $y_{i,1}$ is the location of the generalized inflection point, η runs from zero to one, and s_1 is a stretching parameter that stretches towards $y_{i,1}$ for $s_1 < 1$ and away for $s_1 > 1$. Again, $s_1 = 0.5$ was used. The second "inflection point", $y_{i,2}$, is chosen to be located 3/4 of the distance between $y_{i,1}$ and y_{max}. The stretching parameter s_2 stretches towards y_{max} for $s_2 < 1$ and relaxes the stretching for $s_2 > 1$. Here, $s_2 = 1$ is used. This second exponential grid stretching function gave better grid spacing in the freestream and clustered points near the edge of the computational boundary, which is desirable when a shock coincides with the boundary. The cosine-double-exponential grid retains the benefits of capturing the sharp increases in eigenfunctions at the wall and at the generalized inflection point, while adding additional resolution in the freestream and near the outer edge boundary. Similar to the cosine-exponential case, grid metrics can be computed directly from Eq. 31.

With the grid defined, Eq. 27 can be transformed into computational space and a numerical representation of the derivatives can be given. The first and second derivative operators in the wall-normal direction are discretized by taking derivatives of Lagrange polynomials in physical space. These derivative operators are applied in physical space rather than computational space to avoid Runges phenomena where spurious oscillations can occur for a one-sided stencil with a high order of approximation. Mortensen's[36] scheme can be applied for variable stencil sizes and can be used to obtain high-order approximations. Here, a five-point stencil is used, resulting in a 4th order method similar to the one used by Malik.[3]

After discretization, nonlinearities exist in α so the global method suggested by Malik[3] is used to compute the eigenvalue spectrum with $\alpha^2 = 0$. This method computes the eigenvalues from a generalized eigenvalue problem $\tilde{A}\vec{\phi} = \alpha\tilde{B}\vec{\phi}$ where the LAPACK[48] subroutine ZGGEV is used here for solution. From the eigenvalue spectrum an initial guess can be obtained for the local method which results in $\overline{A}\vec{\phi} = \overline{B}$ and the eigenvalue is found iteratively without dropping the α^2 terms. The LAPACK subroutine ZGESV is used to solve the local problem. It is also possible to avoid the computationally intensive global method and obtain an initial

guess for α from a nearby streamwise location or a DNS simulation assuming the unsteady DNS results are available.

The boundary conditions are required for the freestream and the wall. The wall boundary conditions are linearized non-catalytic conditions for density, no slip, and zero temperature perturbation, although more complex surface boundary conditions can be used for ablation studies.[32,36] In the freestream, a number of boundary conditions were examined. In regions in which the spontaneous radiation of sound does not occur, the perturbations decay rapidly outside of the boundary layer. Therefore, in this case all perturbations are zero except the wall-normal velocity perturbation which is found from the mass conservation equation similar to Stuckert.[49] This type of boundary conditions is hereafter referred to as the "zero" boundary condition, and was used by default unless otherwise specified. In regions of the flow where the spontaneous radiation of sound occurred, a different boundary condition was used that did not force the oscillations at the shock at the outer edge of the domain to zero. The "shock" boundary conditions based on the Rankine-Hugoniot relations were derived, following similar methods as Chang *et al.*[21,50]

The LST shock boundary conditions make the same assumptions as the DNS shock-fitting scheme. The flow upstream of the shock is assumed to be in thermal equilibrium with a fixed chemical composition. The shock is assumed to be infinitely thin, resulting in no relaxation across the shock. In other words, there is no change in chemical composition or vibrational temperature across the shock. The flow surrounding the shock is assumed to be inviscid. The governing equations are transformed into a coordinate system of the shock, illustrated in Figure 3.

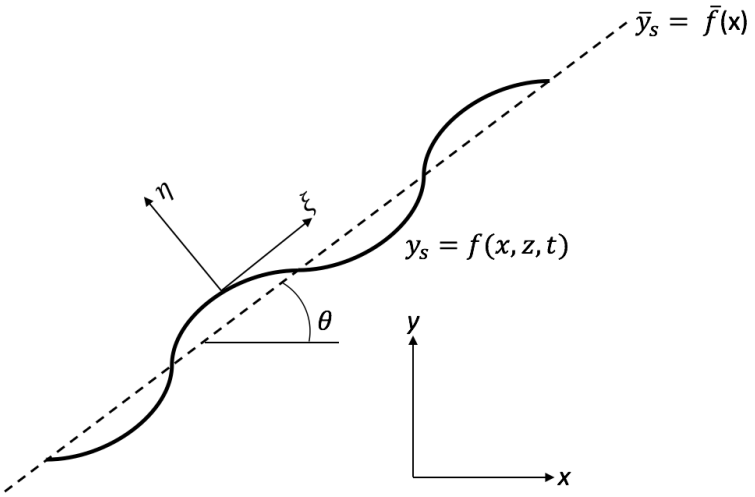

Figure 3: Schematic of unsteady position of a shock in (ξ, η) and (x, y, z) coordinate systems.

The position of the shock in Cartesian coordinates is $y_s = f(x, z, t)$, with the mean shock position $\overline{y_s} = \overline{f}(x)$. Thus the local slope of the shock can be written as

$$a = \tan\theta = \frac{d\overline{f}}{dx}. \tag{34}$$

The transformation between (x, y, z) and (ξ, η) is

$$\xi = \frac{x}{b} \tag{35}$$

$$\eta = b\left[y - f(x, z, t)\right] \tag{36}$$

where $b = \cos\theta$.

Under this transformation, the governing equations become

$$\frac{\partial f}{\partial t}\frac{\partial U}{\partial \eta} - \frac{1}{b^2}\frac{\partial E}{\partial \eta} + \frac{\partial f}{\partial x}\frac{\partial E}{\partial \eta} - \frac{\partial F}{\partial \eta} + \frac{\partial f}{\partial z}\frac{\partial G}{\partial \eta} = 0. \tag{37}$$

Integrating Equation 37 from $\eta = -\epsilon$ to $\eta = \epsilon$ and taking the limit as $\epsilon \to 0$ results in

$$\frac{\partial f}{\partial t}\Delta U + \frac{\partial f}{\partial x}\Delta E - \Delta F + \frac{\partial f}{\partial z}\Delta G = 0 \tag{38}$$

where the Δ terms are the jump conditions across the shock. For example, $\Delta U = U_\infty - U_{shock}$ where the subscript ∞ denotes the conditions immediately upstream of the shock and *shock* denotes conditions immediately downstream of the shock. All flow variables, including f, are perturbed and linearized such that $\phi = \overline{\phi} + \phi'$. Assuming the perturbed variables behave as a normal mode, $\phi' = \hat{\phi} e^{i(\alpha x + \beta z - \omega t)}$, results in

$$\hat{f}\left(-i\omega\Delta\overline{U} + i\alpha\Delta\overline{E} + i\beta\Delta\overline{G}\right) + a\Delta E' - \Delta F' = 0 \tag{39}$$

where

$$\Delta E' = \begin{bmatrix} \overline{\rho_1}\hat{u} + \hat{\rho_1}\overline{u} + \overline{D}_1\left(\overline{c_s}i\alpha\sum_{s=1}^{ns}\hat{\rho}_s - i\alpha\hat{\rho}_1\right) \\ \vdots \\ \overline{\rho_{ns}}\hat{u} + \hat{\rho_{ns}}\overline{u} + \overline{D}_{ns}\left(\overline{c_s}i\alpha\sum_{s=1}^{ns}\hat{\rho}_s - i\alpha\hat{\rho}_{ns}\right) \\ \hat{\rho}\overline{u}^2 + 2\overline{\rho u}\hat{u} + \hat{p} \\ \hat{\rho}\overline{u}\overline{v} + \overline{\rho v}\hat{u} + \overline{\rho u}\hat{v} \\ \hat{\rho}\overline{u}\overline{w} + \overline{\rho w}\hat{u} + \overline{\rho u}\hat{w} \\ \hat{u}\left(\overline{\rho e} + \overline{p}\right) + \overline{u}\left(\hat{\rho e} + \hat{p}\right) \\ \overline{\rho e_v}\hat{u} + \rho\hat{e}_v\overline{u} \end{bmatrix}, \tag{40}$$

$$\Delta F' = \begin{bmatrix} \overline{\rho_1}\hat{v} + \hat{\rho_1}\overline{v} \\ \vdots \\ \overline{\rho_{ns}}\hat{v} + \hat{\rho_{ns}}\overline{v} \\ \hat{\rho}\overline{u}\overline{v} + \overline{\rho v}\hat{u} + \overline{\rho u}\hat{v} \\ \hat{\rho}\overline{v}^2 + 2\overline{\rho v}\hat{v} + \hat{p} \\ \hat{\rho}\overline{v}\overline{w} + \overline{\rho w}\hat{v} + \overline{\rho v}\hat{w} \\ \hat{v}\left(\overline{\rho e} + \overline{p}\right) + \overline{v}\left(\hat{\rho e} + \hat{p}\right) \\ \overline{\rho e_v}\hat{v} + \rho\hat{e}_v\overline{v} \end{bmatrix} \tag{41}$$

where

$$\hat{\rho} = \sum_{s=1}^{ns}\hat{\rho}_s \tag{42}$$

$$\hat{p} = \sum_{s=1}^{ns}\left(\overline{\rho}_s\frac{\mathcal{R}}{M_s}\hat{T} + \hat{\rho}_s\frac{\mathcal{R}}{M_s}\overline{T}\right) \tag{43}$$

$$\hat{\rho e} = \sum_{s=1}^{ns}\left(\overline{\rho}_s c_{v,s}\hat{T} + \hat{\rho}_s c_{v,s}\overline{T}\right) + \rho\hat{e}_v + \frac{1}{2}\hat{\rho}\overline{u_i}^2 + \overline{\rho u_i}\hat{u}_i\sum_{s=1}^{ns}\hat{\rho}_s h_s^o \tag{44}$$

$$\rho\hat{e}_v = \sum_{s=1}^{ns}\left(\hat{\rho}_s\overline{e}_{vs} + \overline{\rho}_s\frac{\partial e_{vs}}{\partial\overline{T}_V}\hat{T}_V\right) \tag{45}$$

Note that now Equation 39 introduces an extra perturbation variable $\hat{f}$. To eliminate the extra variable, $\hat{f}$ is solved for in terms of the other perturbation variables using the x-momentum equation. However, this reduces the system to $ns+4$ equations for $ns+5$ independent perturbation variables. The $ns+4$ equations can be represented by

$$\sum_{j=1}^{ns+5}\hat{B}_{ij}\hat{\phi_j} = 0, \quad i = 1, 2, \ldots, ns+4 \tag{46}$$

where the terms in $\hat{B}$ are included in the Appendix.

To close the system of equations for the shock boundary conditions, an extra equation is needed, for which there are a number of options. The mixture continuity equation, y-momentum equation, and the right-running characteristic equation derived from the 2D Euler equations for a perfect gas were all explored as the closure equation for the shock boundary conditions. There were only minimal differences in results depending on which closure equation was used. However since the y-momentum equation was already cast

into the LST framework and hard-coded into the LST program, it was the simplest closure equation to implement yet also produced the smoothest solution near the shock. Therefore, the y-momentum equation was used as the shock boundary condition closure equation.

It should be noted that these freestream boundary conditions differ significantly from the method used by Bitter and Shepherd,[9] who use Mack's[51] method determine the asymptotic behavior of the solutions in the freestream and integrate toward the wall using a Runge-Kutta method. This allows Bitter and Shepherd[9] to use a much smaller computational domain and still capture the oscillatory behavior of the eigenfunctions when the disturbance is traveling supersonically relative to the freestream. However, despite the differences in mathematical techniques, the LST performed here produces similar results.

LST gives information about what disturbance frequencies are unstable and the corresponding growth rates of those frequencies, but there is no information on the amplitude of the incoming disturbance. To estimate boundary-layer transition using LST, the e^N transition criterion is used which is defined as

$$e^N = \frac{A(s)}{A_0} = \exp\left[\int_{s_0}^{s} -\alpha_i(s,f)ds\right] \tag{47}$$

where $A(s)$ is the integrated disturbance amplitude, A_0 is the initial disturbance amplitude, s_0 is the location where the disturbance first becomes unstable, and α_i is the spatial amplification rate obtained from LST. The integration is performed for a constant frequency f, and is done numerically using trapezoidal integration. Note that a negative imaginary part of the wave number α results in disturbance growth while a positive value results in disturbance decay. The N-factor is specifically the exponent of e^N. In-flight transition N-factors are commonly understood to be around 10. Malik[11] showed that 9.5 and 11.2 correlated with transition onset for two high Mach number flight tests. In ground test facilities the transition N-factor is usually lower.

V. Results

Steady DNS translation-rotation temperature, vibration temperature, and mass fraction contours for the nose region of the cone are shown in Figure 4. Figures 4(a) and (b) indicate the flow is in thermal nonequilibrium in the nose region, and Figures 4(c) and (d) indicate the flow is in chemical nonequilibrium. Specifically, O_2 dissociation is the predominant reaction in this flow field, whereas N_2 does not dissociate as severely. Similar contours are shown in Figure 5 for a downstream region of the cone. Due to the cold wall, the boundary layer is thin in relation to the flow domain. Although it may appear that the flow outside of the boundary layer is in thermal equilibrium, closer inspection reveals otherwise.

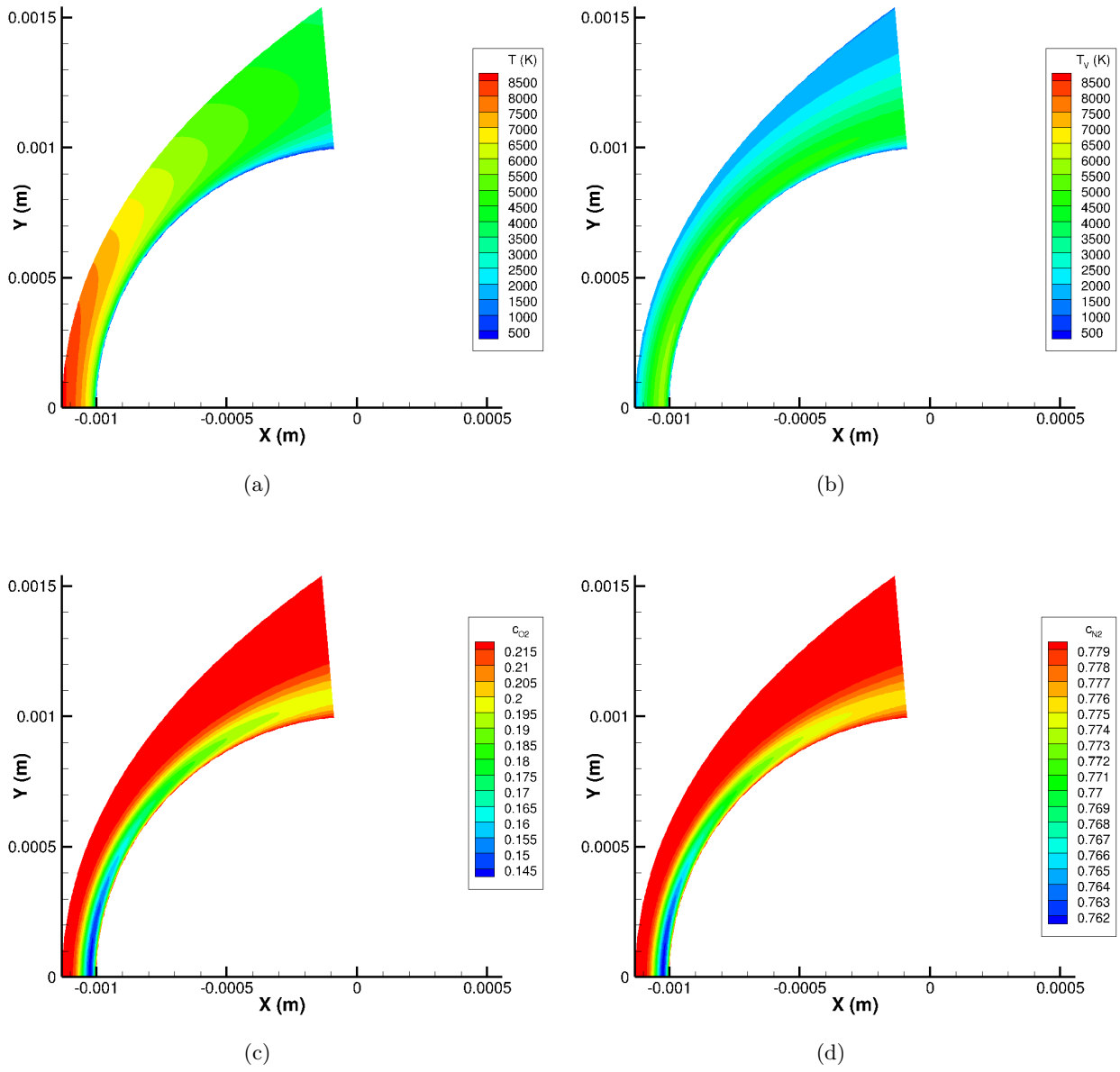

Figure 4: Steady DNS contours in nose region. (a) T. (b) T_V. (c) Mass fraction of O_2. (d) Mass fraction of N_2.

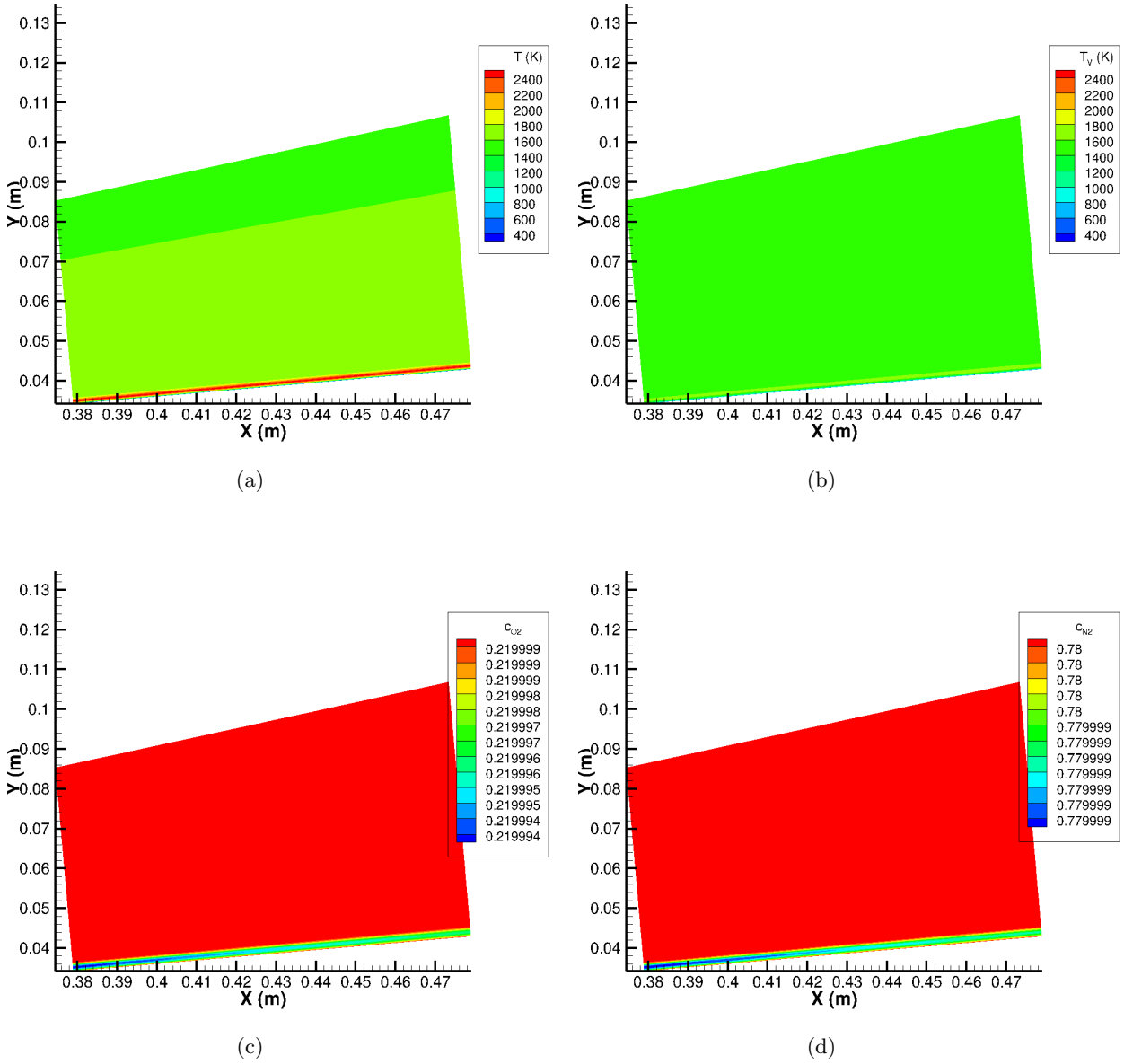

(a) (b)

(c) (d)

Figure 5: Steady DNS contours in a downstream region. (a) T. (b) T_V. (c) Mass fraction of O_2. (d) Mass fraction of N_2.

Figure 6 shows the boundary layer profiles for temperature, vibration temperature, tangential velocity, and species density of N_2 and O_2 at a streamwise distance from the stagnation point of $s = 0.4$ m. Hereafter, y denotes the wall-normal distance. The meanflow does not reach thermal equilibrium in the free stream, thus demonstrating the necessity of accounting for nonequilibrium effects in these types of flows. The mass fractions of N_2 and O_2 follow the same trend in the boundary layer, but do not vary greatly in magnitude from their freestream values in these flow conditions. Although the effect of chemical nonequilibrium in the meanflow may be small, it may still have an effect in LST calculations.

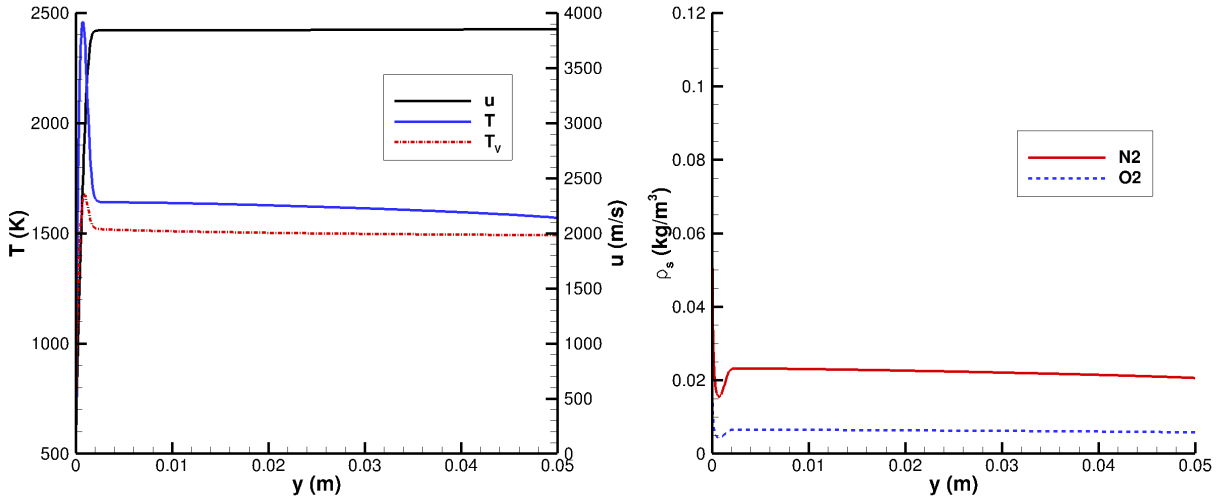

(a) (b)

Figure 6: Meanflow boundary layer profiles at $s = 0.4$ m ($R = 830$). (a) u, T, and T_V. (b) Species density ρ_s of N_2 and O_2 species. u denotes the component of velocity tangential to the surface of the cone. y is the wall normal distance.

A. LST Results

LST was performed to determine which modes were unstable. All LST calculations performed here assume a spanwise wavenumber of $\beta = 0$. Unless otherwise stated, 300 wall-normal grid points were used and the "zero" freestream boundary condition was used. The global method, which assumes $\alpha^2 = 0$, was used at a fixed streamwise location and frequency to obtain an initial guess for the eigenvalues of the physical modes. The local method, which does not neglect α^2, then used this initial guess and iterated to a converged solution. Once the eigenvalues of a physical mode have been obtained, it is possible to march in the streamwise direction using the eigenvalues from the previous location as an initial guess. At each streamwise location, the spatial growth rate is given by the negative of the imaginary component of the eigenvalue ($-\alpha_i$), and the phase speed is calculated from the real component of α. The nondimensional phase speed is defined as $c_r = \frac{(\omega^*/u^*_\infty)}{\sqrt{\beta^2+\alpha_r^2}}$, where $\omega^* = 2\pi f$ is the dimensional circular frequency and u^*_∞ is the freestream velocity upstream of the shock. Traditionally, the streamwise distance is presented in nondimensionalized form as the Reynolds number, R, and frequency as F. Additionally, the growth rate is typically nondimensionalized by L^*.

$$R = Re_x^{1/2} = \sqrt{\frac{\rho^*_\infty u^*_\infty s}{\mu^*_\infty}} = \frac{\rho^*_\infty u^*_\infty L^*}{\mu^*_\infty} \tag{48}$$

$$L^* = \sqrt{\frac{\mu^*_\infty s}{\rho^*_\infty u^*_\infty}} \tag{49}$$

$$F = \frac{\omega^* \mu^*_\infty}{\rho^*_\infty u^{*2}_\infty} \tag{50}$$

The relation between R, F, and the nondimensional frequency Ω is simply

$$\Omega = RF. \tag{51}$$

The freestream conditions were

$$u^*_\infty = 3.388E+03 \text{ m/s}, \quad \rho^*_\infty = 2.322E-02 \text{ kg/m}^3, \quad \mu^*_\infty = 5.244E-05 \text{ kg m/s}.$$

A phase speed and growth rate plot in the style of Ma and Zhong[52] is shown in Figure 7 for a frequency of $F = 9.41E-4$ ($f = 1$ MHz). In hypersonic boundary layer stability, there are a number of physical modes that are not present in lower speed flows. Mode F1, F2, and higher modes originate in the fast acoustic spectrum - a continuous spectrum of eigenvalues whose branch cut begins at a phase speed of approximately $c_r = 1 + 1/Ma$ where Ma is the meanflow Mach number outside the boundary layer. Mode S, commonly referred to as Mack's mode, originates in the slow acoustic spectrum - a continuous spectrum of eigenvalues whose branch cut begins at a phase speed of approximately $c_r = 1 - 1/Ma$. Two other continuous spectra of interest, the entropy and vorticity spectra, have phase speed of approximately $c_r = 1$, and can cause instabilities when synchronizing with the discrete modes (F1, F2, S, etc.). Mack's second mode instability typically occurs downstream of the synchronization point, which is defined as the point where modes F1 and S have the same phase speed. Following synchronization of modes F1 and S, it is possible for either mode to become unstable ($-\alpha_i > 0$), while the other remains stable ($-\alpha_i < 0$). The results in Figure 7 indicate that mode F1 becomes unstable, while mode S is stable. It is conventional to describe the unstable mode as "Mack's second mode," even though mode S is stable here. Therefore, all references to the second mode hereafter indicate the mode F1 instability. Mode F1 becoming the dominant instability is consistent with Bitter and Shepherd.[9]

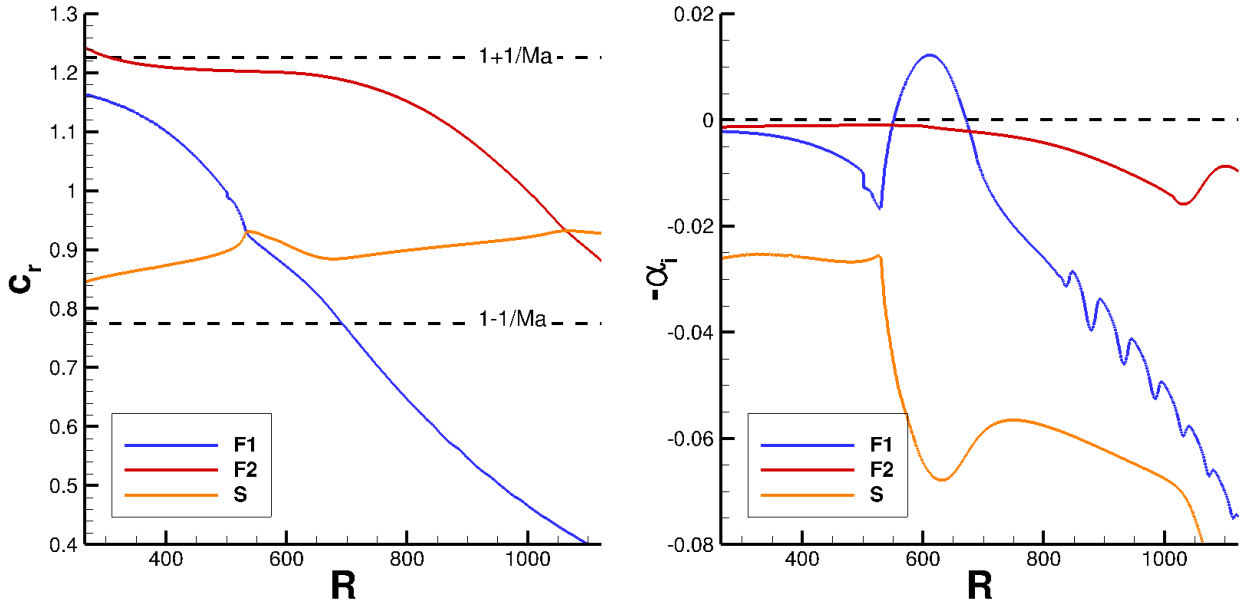

(a) (b)

Figure 7: LST phase speed and nondimensional growth rate for Modes F1, F2, and S at $F = 9.41E-4$ ($f = 1$ MHz). (a) Phase Speed. (b) Growth Rate.

In order to determine in which frequency and Reynolds number ranges mode F1 is unstable, the streamwise marching procedure was repeated for a number of frequencies, producing the neutral stability map for the second mode in Figure 8. This map indicates the locations and frequencies in which a disturbance grows. Neutrally stable points ($-\alpha_i = 0$) are shown as the thick black line. All points inside of the curve formed by the neutral points have positive growth rates. At frequencies below $F = 7.5E-04$ (corresponding to roughly $f = 800$ kHz) and Reynolds numbers greater than $R = 830$ (corresponding to streamwise locations approximately greater than $s = 0.4$ m), shown by the region inside the white box in Figure 8, the region of instability broadens. Bitter and Shepherd[9] noted the unstable supersonic modes increase the range of instability, therefore this particular region on the neutral stability curve was examined in finer detail through growth rate and phase speed plots for individual frequencies to determine whether or not the supersonic unstable modes were present.

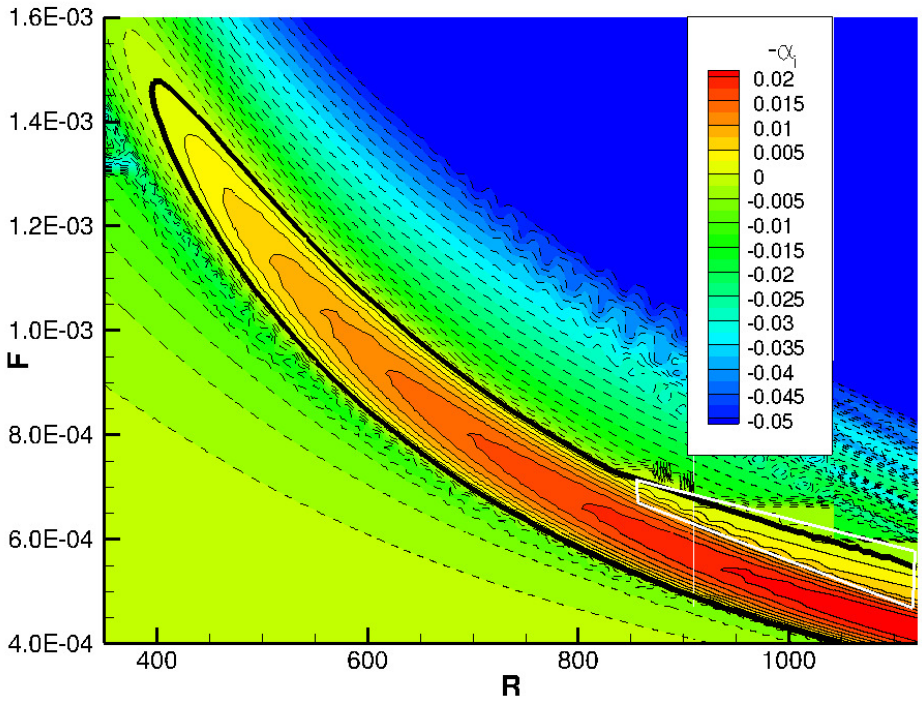

Figure 8: Neutral stability map for second mode. Dashed lines indicate negative growth rates. Thick black line indicates points of neutral stability. White box indicates region of supersonic mode.

Supersonic unstable modes were found for frequencies below $F = 7.53E-04$. The growth rate and phase speed plots for a number of unstable supersonic modes are shown in Figure 9. Similar to Bitter and Shepherd,[9] the mode branches into two distinct modes upon synchronization with the slow acoustic spectrum, indicated by the kink in the growth rate plots. Following similar notation to Bitter and Shepherd[9] and Fedorov and Tumin,[53] the unstable mode is denoted as $F1^+$, and the new stable mode as $F1^-$. Synchronization with the slow acoustic spectrum causes mode $F1^+$ to change from a discrete mode to a continuous mode and simultaneously creates the discrete mode $F1^-$. The major difference between discrete and continuous modes is the behavior of the eigenfunctions in the freestream. Discrete modes have eigenfunctions which decay in amplitude outside of the boundary layer, whereas continuous modes have oscillatory behavior in the free stream. From Figure 9, mode $F1^+$ (solid line) remains unstable for longer along the streamwise distance, which may lead to transition earlier on the body. After becoming stable, mode $F1^+$ ceases to exist and merges with the slow acoustic continuous spectrum, as it does in results presented by Bitter and Shepherd.[9] Mode $F1^-$ (dotted line) becomes increasingly stable downstream, but exhibits a similar eigenfunction to mode $F1^+$ at first, as shown in Figure 10 for $F = 5.18E-04$ and $R = 1120$. The pressure eigenfunction is scaled by local flow values and is equal to unity at the wall. The axis limits for the eigenfunctions shown in Figure 10 are modified to show details in each oscillatory region. For both the unstable and stable modes, the fluctuations in the eigenfunctions extend well into the freestream, similar to results presented by Bitter and Shepherd.[9] Due to the oscillatory nature of the eigenfunctions in the freestream, the effect of the "shock" freestream boundary conditions versus the "zero" boundary conditions was examined here. However, due to the the large computational zone, the perturbation is very weak at the shock boundary. For this reason there was no difference visible on the scale of the plot between the zero boundary condition and the shock boundary condition, provided the grid resolution is high (at least 1500 grid points in this case). The shock boundary conditions with grid stretching near the shock allowed for fewer grid points to be used, saving computational cost. For all subsequent analyses of the supersonic modes, the shock boundary conditions were used.

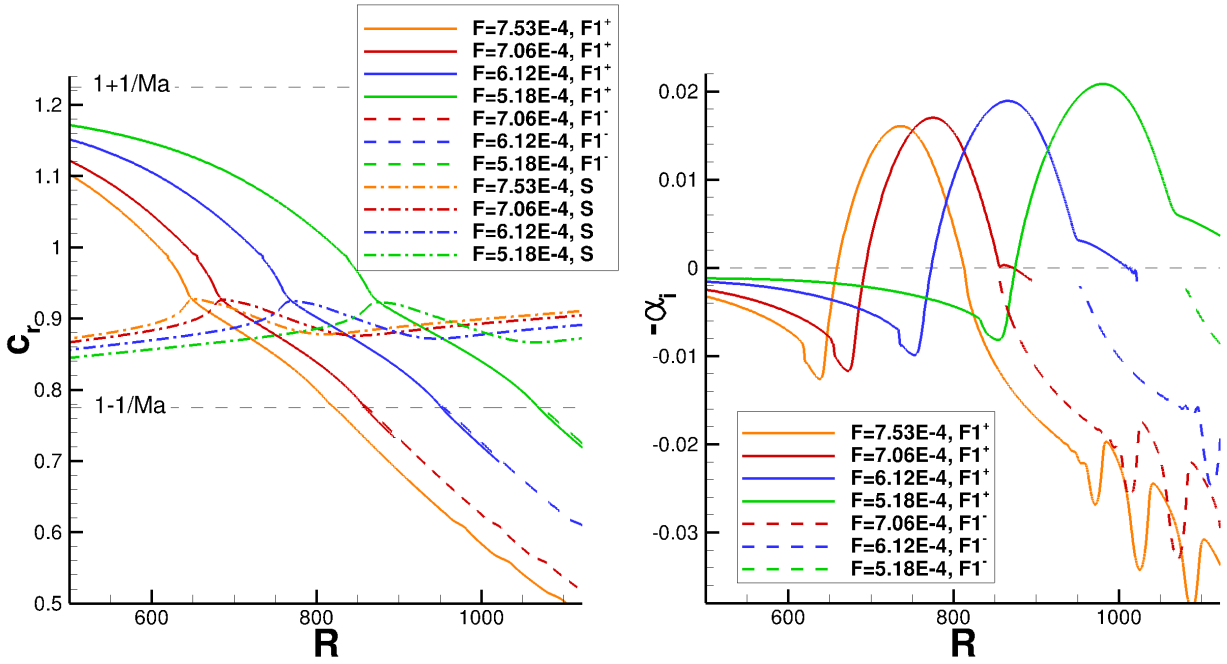

(a) (b)

Figure 9: LST phase speed and nondimensional growth rate for supersonic unstable modes. (a) Phase Speed. (b) Growth Rate. Dashed lines indicate the new modes created by synchronization with the slow acoustic spectrum.

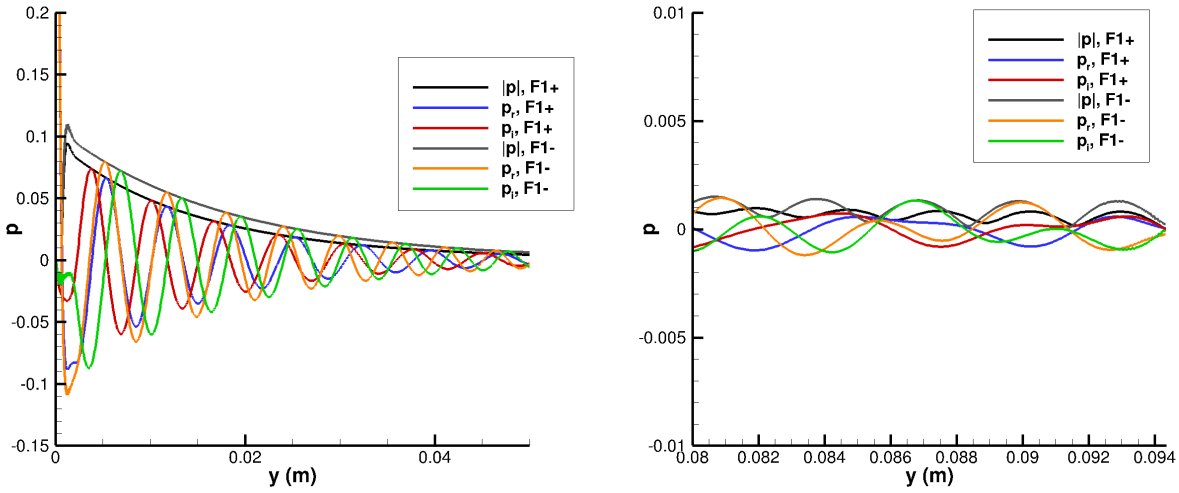

(a) (b)

Figure 10: Pressure eigenfunction normalized by local pressure for unstable and stable supersonic mode branches at $F = 5.18E-04$ and $R = 1120$. Phase speed and growth rate for Mode F1$^+$: $c_r = 0.717$, $-\alpha_i = 3.47E-3$. Mode F1$^-$: $c_r = 0.728$, $-\alpha_i = -6.90E-3$. (a) Highly oscillatory boundary layer region. (b) Weakly oscillatory region near the shock.

In visualizing the merging of mode F1$^+$ with the slow acoustic continuous spectrum, it is instructive to examine the dispersion relation shown in Figure 11. The data are exactly the same as in Figure 9,

however the dispersion relation shows the relationship between the nondimensional phase speed c_r and the nondimensional growth rate $-\alpha_i$. Also shown in Figure 11 are the slow acoustic and entropy/vorticity continuous spectra, which are a function of frequency, Reynolds number, and Mach number in the free stream. Further discussion of the continuous spectra and their calculation is available from Balakumar and Malik[54] and Tumin.[55–57] It should be noted that the continuous spectra calculations performed here are for a perfect gas and may not be entirely representative of this flow field. They are intended to be used as an approximation for visualizing synchronization. Mode F1$^+$ begins in the fast acoustic continuous spectrum (not pictured) and decreases in phase speed as Reynolds number R increases. Near $c_r = 1$, the second mode synchronizes with the continuous entropy/vorticity spectra (which are actually two overlapping branches). This interaction with the continuous modes causes a damping effect in mode F1$^+$. Fedorov and Tumin[58] note that the boundary layer is particularly receptive to entropy/vorticity disturbances in this synchronism region. Further downstream, the mode becomes unstable. The point at which the mode first becomes unstable corresponds to the lower neutral branch on the stability curve. As R increases, the mode behaves differently for lower frequencies. At $F = 7.53E-4$ and above, the mode becomes stable before synchronizing with the slow acoustic spectrum ($c_r = 1-1/Ma$). The point at which the second mode becomes stable again corresponds to the upper branch of the neutral stability curve. The lower frequencies, however, synchronize while still unstable. This causes the cessation of mode F1$^+$ being discrete, and causes the creation of the new discrete mode F1$^-$, shown by the dotted line in Figure 11. Mode F1$^+$ remains unstable for longer along the body until it finally becomes stable and merges with the rest of the slow acoustic continuous spectrum. This delay in mode F1$^+$ becoming stable is visualized in the broadening of the region of instability, shown by the white box on the neutral stability map in Figure 8. The synchronization of mode F1$^+$ with the slow acoustic spectrum is akin to the synchronization with the entropy/vorticity modes. Similarly, the boundary layer may be receptive to slow acoustic disturbances in the free stream near this region. However, as Bitter and Shepherd[9] have pointed out, since the synchronism region is near the upper branch of the neutral curve, it is unlikely to cause significant amplifications to the second mode.

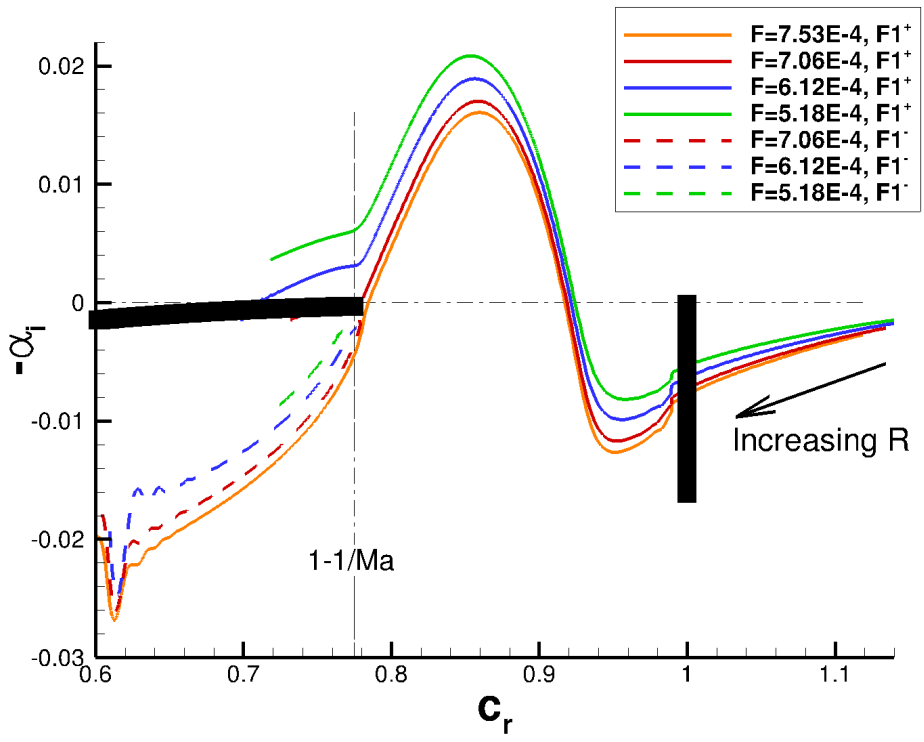

Figure 11: Dispersion relation for second mode. Thick black lines correspond to the continuous spectra evaluated at $Ma = 4.44$, $R = 1000$, and $\Omega = RF = 0.4$. Dashed lines indicate the new mode F1$^-$ created during synchronization with the slow acoustic spectrum.

The mode F1$^+$ growth rate for each frequency was integrated along the surface numerically using the trapezoidal method to determine the N-factor curve for this particular case. The N-factor, $N = \ln(A/A_0)$, is presented as a function of Reynolds number R. Frequency increments of $\Delta F = 4.707E-8$ ($\Delta f = 50$ kHz) were used to obtain the N-factor results in Figure 12. The maximum Reynolds number for this case due to the length of the cone is approximately $R = 1300$. An N-factor of roughly 7 will be achieved by the end of the length of the 1 meter cone. Note the influence of the supersonic modes in changing the shape of the peaks of the N-factor for each frequency. For example, at $F = 5.65E-4$, the peak does not appear as smooth as the peak for $F = 9.41E-4$. The curve is elongated due to mode F1$^+$ being unstable. These supersonic modes seem to have only a small impact on the edge of the N-factor curve, however, as shown by the green line in Figure 12. The maximum N-factor for at particular Reynolds number is encountered before the maximum N-factor for the corresponding frequency. That is, for example, at $R = 1000$, the N-factor is $N = 5.13$ due to the amplification at the frequency $F = 5.65E-4$. However, the maximum N-factor value for $F = 5.65E-4$, which is $N = 5.63$, is encountered at $R = 1100$, yet the highest N-factor at $R = 1100$ is approximately $N = 6.15$. The largest influence of the supersonic mode comes between $R = 1000$ and $R = 1100$ for $F = 5.65E-4$, yet it does not have an impact on the maximum N-factor. Therefore, the supersonic modes contribute very little to the maximum N-factor for this case. However, because this N-factor curve is only valid for the flow conditions in Case 1, it is difficult to draw a definitive conclusion on the role of the supersonic modes in N-factor transition prediction methods. More cases with different flow conditions are necessary to evaluate the effect of the spontaneous radiation of sound on transition using the e^N method.

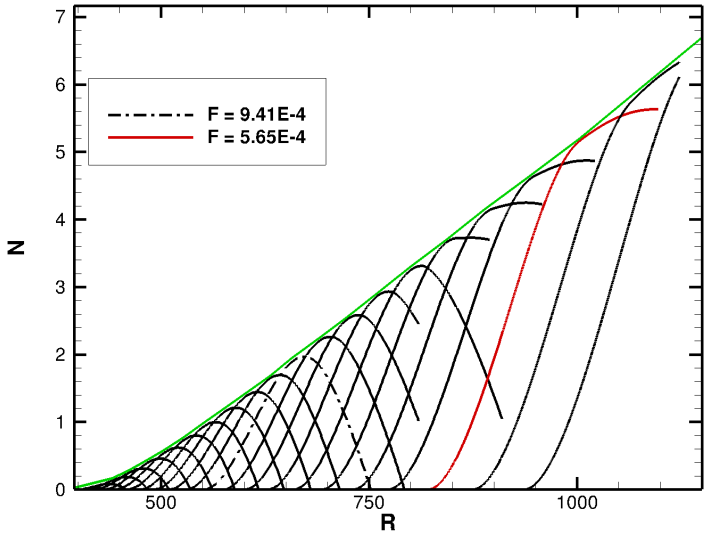

Figure 12: N-factor for unstable second mode frequencies. Frequencies are in increments of $\Delta F = 4.707E-8$ ($\Delta f = 50$ kHz). The green line is an approximation of the edge of the N-factor curve.

To provide a qualitative visual comparison with the unsteady DNS results, the perturbation contour predicted by LST was created. At each streamwise location, the eigenfunction $\hat{\phi}$ and eigenvalue α were obtained from the local LST method. The wall-normal eigenfunction at each streamwise location represents the normalized perturbation in ϕ at that location. These perturbations are then assembled into a 2D contour of perturbations. For example, the pressure perturbation field is expressed explicitly as

$$p'(x,y) = Real\left[\hat{p}(x,y)e^{i(\alpha(x)x+\beta z-\omega t)}\right] \tag{52}$$

where $\alpha(x)$ is the complex wavenumber at streamwise location x, and $\hat{p}(x,y)$ is the complex pressure eigenfunction at each streamwise location. The pressure perturbation contour at time $t = 0$ is shown in Figure 13. A similar contour was created for the temperature perturbations, also shown in Figure 13. It should

be noted that the pressure and temperature contours have been locally scaled by their absolute maximum value at each streamwise location.

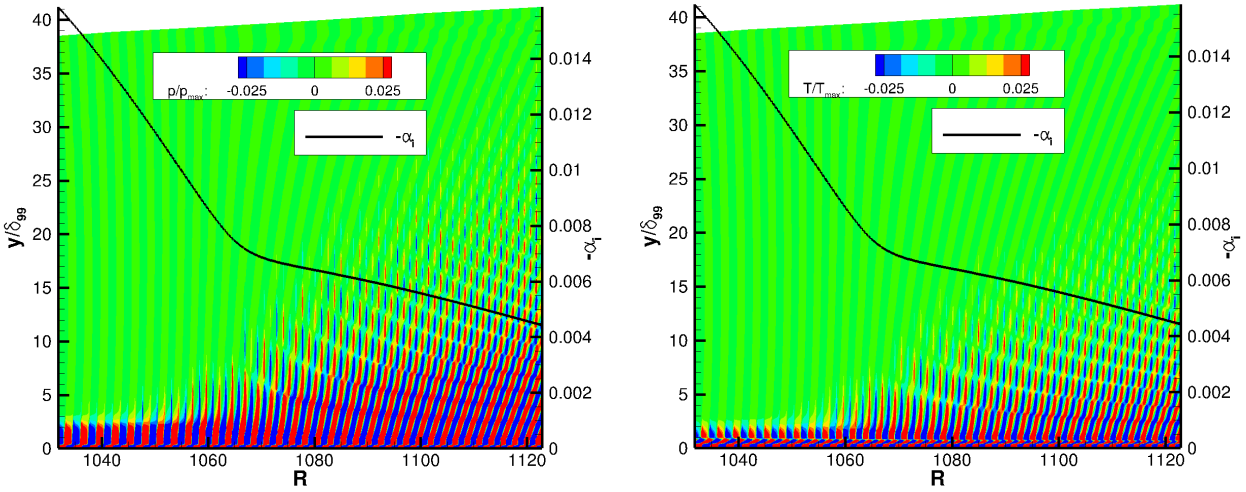

(a) (b)

Figure 13: LST perturbation contours at $F = 5.18E-4$ ($f = 550$ kHz). (a) Pressure perturbation. (b) Temperature perturbation. Contours have been locally scaled by their absolute maximum value at each streamwise location. Wall-normal distance has been scaled by the local boundary layer thickness δ_{99}.

The growth rate has been overlayed in Figure 13 to illustrate the fundamental difference in the perturbation field after synchronization with the slow acoustic spectrum (indicated by the "kink" in the growth rate). Prior to synchronization, the perturbations are largely confined to within the boundary layer and the angle created by the perturbation with respect to the wall is perpendicular. As the second mode synchronizes with the slow acoustic spectrum, the perturbation begins to grow into the freestream outside of the boundary layer, and the angle created by the perturbations moves gradually from perpendicular towards the wall in the clockwise direction. Additionally, the vertical component of the energy flux vector of the perturbation outside of the boundary layer is positive, i.e. $e_y = (\hat{v}_r\hat{p}_r + \hat{v}_i\hat{p}_i)/2 > 0$. This indicates the radiation of sound away from the wall.

Lastly, the temperature perturbation contour predicted by LST for a fixed wavenumber and frequency was created to demonstrate the role of the relative Mach number (Eq. 1) in flows with the supersonic mode. The contour in Figure 14 is obtained from Eq. 52, however α is the complex wavenumber at the fixed streamwise location s_0 and frequency f_0 and $\hat{T}$ is the complex temperature eigenfunction at the fixed streamwise location s_0 and frequency f_0. The streamwise distance s is varied only slightly because in general, α and $\hat{p}$ are functions of s, making this technique invalid for regions far from s_0. The temperature perturbation contour at time $t = 0$ in Figure 14 illustrates very clearly the distinct regions of the disturbance behavior summarized by the supersonic mode diagram in Figure 2. For both the subsonic and supersonic modes, the first sonic line $M_r = -1$ acts as a wave guide for the acoustic waves traveling downstream supersonically relative to the meanflow velocity. Centered about $M_r = 0$, the "rope-like" wave structures can be seen for both the supersonic and subsonic modes. However, outside of these "rope-like" wave structures is where the subsonic and supersonic modes differ fundamentally. For the subsonic mode (Fig. 2(a)), the relative Mach number does not exceed $M_r = 0.6$, meaning the disturbance is traveling subsonically with respect to the meanflow velocity for the entirety of the flow field outside of the boundary layer. The relative Mach number for supersonic mode (Fig. 2(b)), on the other hand, exceeds $M_r = 1$ near the edge of the boundary layer. This means the disturbance is traveling upstream supersonically with respect to the meanflow velocity. The effect of this supersonic disturbance propagation is the "slanted" wave pattern in the freestream. Indeed, the angle this wave pattern makes agrees with the predicted Mach angle $\mu = \arcsin(1/M_r) = 50.3°$.

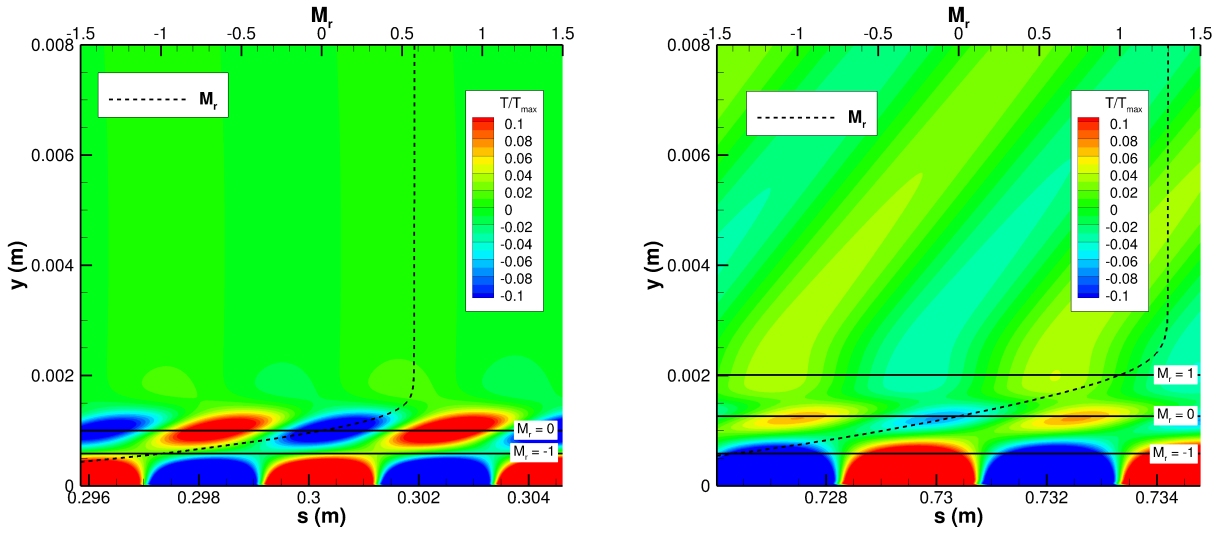

(a) (b)

Figure 14: LST pressure perturbation contours. (a) Subsonic mode: $s = 0.302$m, $f = 800$ kHz. (b)Supersonic mode: $s = 0.733$m, $f = 550$ kHz.

The results presented in this section indicate that the LST numerical methods used are capable of capturing the unique physics that occur when the second mode is unstable and traveling supersonically with respect to the free stream. The supersonic mode has been shown to be the result of mode F1 synchronizing with the slow acoustic spectrum, splitting mode F1 into a stable mode $F1^-$ and a unstable mode $F1^+$. The relative Mach number has been shown to be a critical parameter in the structure of the boundary layer disturbances. Specifically, below $M_r = -1$ the disturbance travels downstream supersonically with respect to the meanflow and is confined by the sonic line. Between $M_r = -1$ and $M_r = 1$, the disturbance travels subsonically with respect to the meanflow, resulting in "rope-like" structures. For supersonic modes, there exists a second sonic line at $M_r = 1$, outside of which the disturbance travels upstream supersonically with respect to the meanflow, resulting in "slanted" wave patterns at an angle $\mu = \arcsin(1/M_r)$. Further analysis through unsteady DNS was performed to verify the phenomena predicted by the LST analysis.

B. Unsteady DNS Results

To study stability using DNS, it is required that the meanflow be perturbed in order to study the growth, or decay, of the perturbation. Here, the flow is perturbed with a suction/blowing slot at the cone surface. The equation for the mass flux of the slot is

$$\rho v(x,t)'_w = \epsilon_b (\rho u)_\infty \exp\left\{-\frac{(t-\mu_b)}{2\sigma_b^2}\right\} \sin\left\{\frac{2\pi(x-x_b)}{l_b}\right\} \tag{53}$$

where l_b is the length of the slot, x_b is the center of the slot measured from the leading edge of the cone, ϵ_b scales the function, μ_b shifts the Gaussian component to avoid negative times, and σ_b adjusts the spectral content of the function. Notice the time dependent Gaussian portion of the function. When transformed to frequency space, this yields a continuous range of frequencies with non-zero amplitudes making this particular approach for perturbing the meanflow an effective strategy when studying a wide range of frequencies.

The pulse parameters are summarized in Table 2. The frequency spectrum of the pulse is presented in Figure 15. The Fourier transform indicates the majority of the frequency content of the pulse is below 1MHz. From the LST analysis, it was predicted that the unstable supersonic modes will be present below this frequency. The amplitude of the perturbation is small enough that the disturbance is approximately linear.

Table 2: Gaussian pulse parameters for DNS.

ϵ_b	μ_b	σ_b	x_b	l_b
$1E-4$	$3E-6$	$4E-7$	$0.1m$	$0.002m$

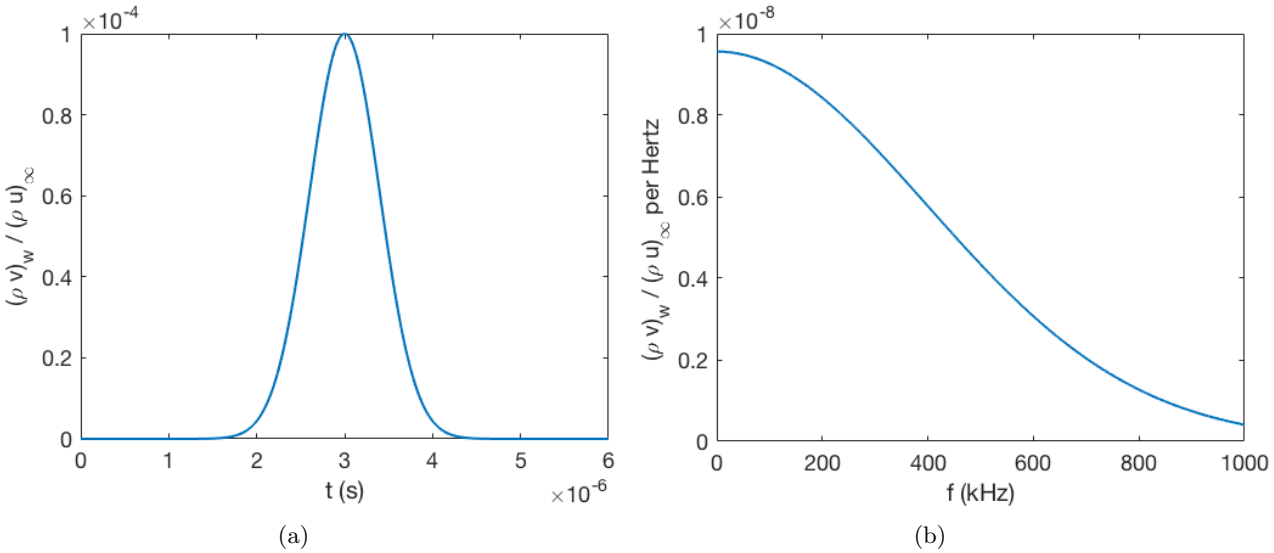

(a) (b)

Figure 15: Gaussian pulse for unsteady DNS. (a) Nondimensional mass flux amplitude. (b) Frequency content of pulse.

The evolution of the Gaussian pulse downstream is visualized in Figure 16 using snapshots in time of contours of the pressure perturbation normalized by the local meanflow pressure ($\frac{\Delta p}{p}$). The same value at the surface of the cone is included to more clearly visualize the growth of disturbances. The traditional second mode growth can be seen in Figure 16(a) in particular between $x = 0.3$ m and $x = 0.45$ m. The start of the spontaneous radiation of sound appears in Figure 16(b) between $x = 0.35$ m and $x = 0.4$ m. When the pulse travels to approximately $x = 0.5$m, the spontaneous radiation of sound becomes much more apparent, shown in Figure 16(c). The supersonic modes continue to grow into the freestream as the pulse continues downstream (Figures 16(d)-(f)). The perturbations near the upper boundary in Figure 16(a) and (b) are a result of the Mach wave from the pulse traveling downstream and eventually interacting with the shock. These interactions are weak, however, and disperse before the spontaneous radiation of sound occurs.

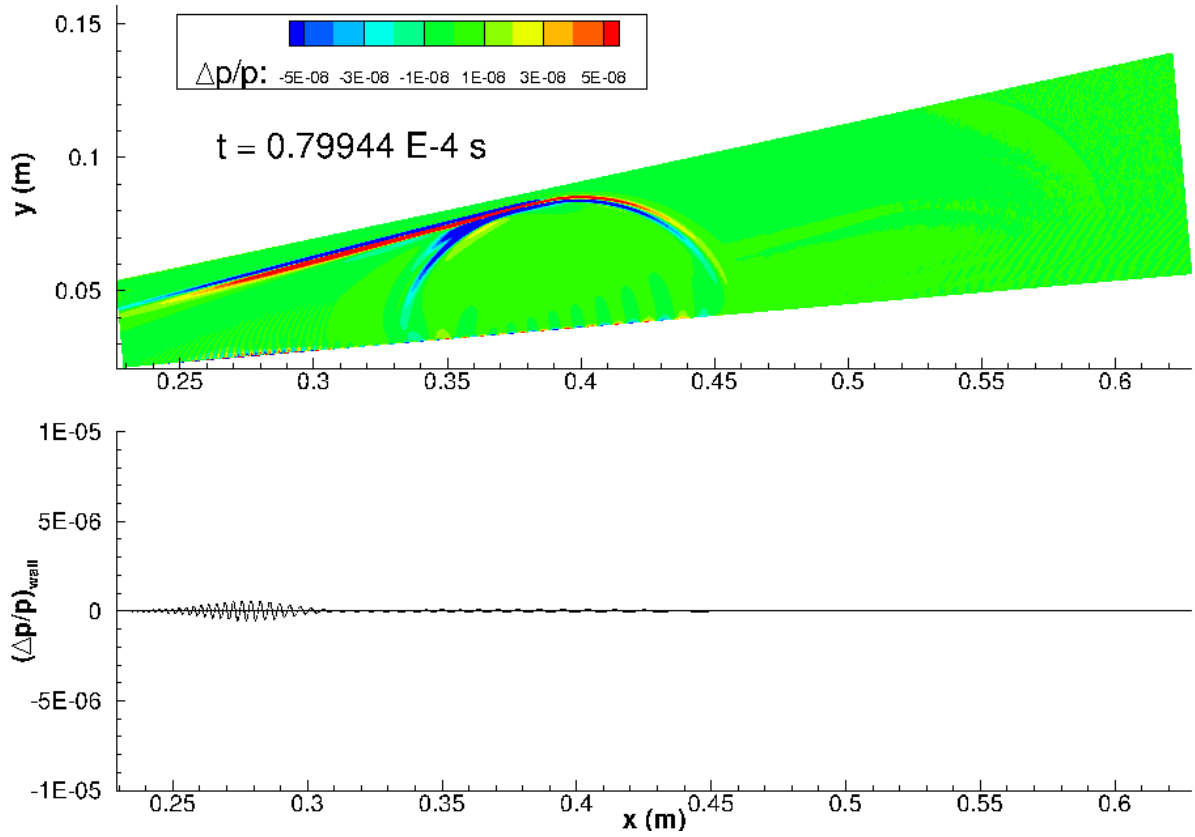
△p/p: -5E-06 -3E-06 -1E-06 1E-06 3E-06 5E-06
t = 0.79944 E-4 s
y (m)
0.15
0.1
0.05
0.25
0.3
0.35
0.4
0.45
0.5
0.55
0.6
1E-05
5E-06
0
-5E-06
-1E-05
(△p/p)wall
x (m)

(a)

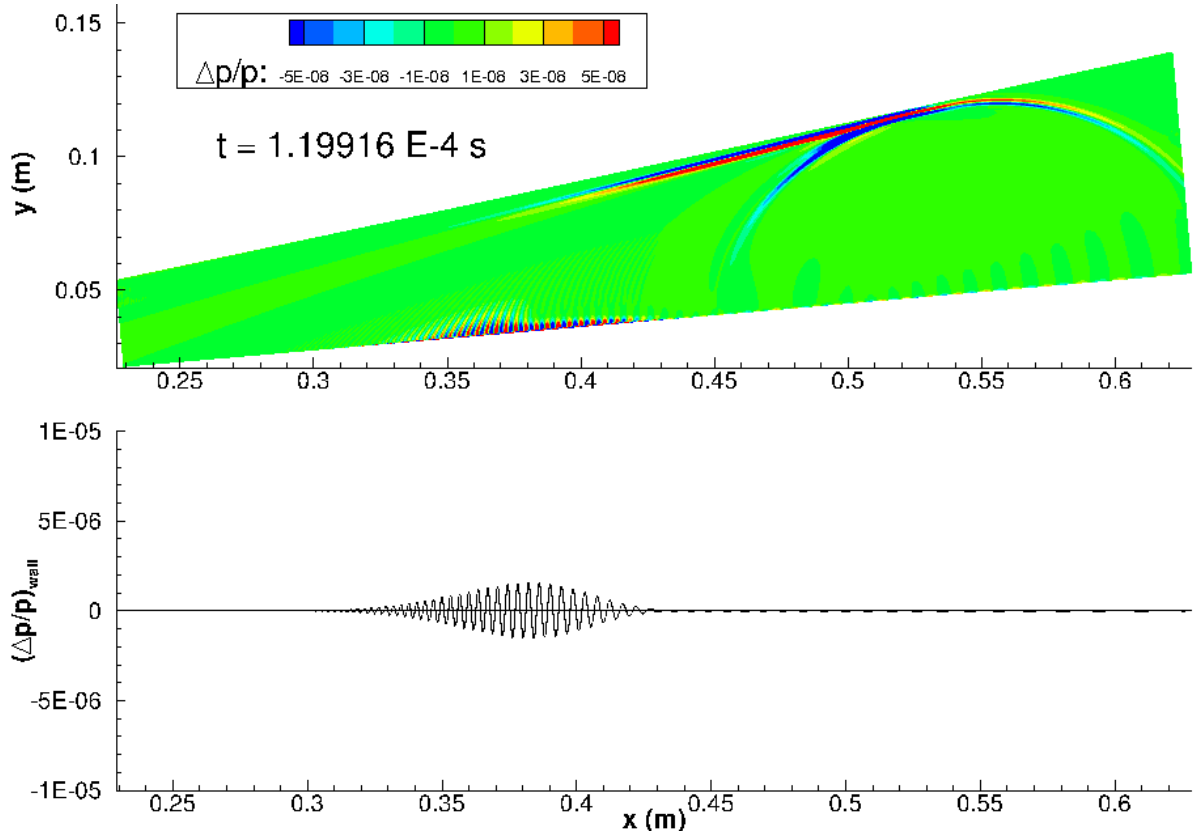
△p/p: -5E-06 -3E-06 -1E-06 1E-06 3E-06 5E-06
t = 1.19916 E-4 s
y (m)
0.15
0.1
0.05
0.25
0.3
0.35
0.4
0.45
0.5
0.55
0.6
1E-05
5E-06
0
-5E-06
-1E-05
(△p/p)wall
x (m)

(b)

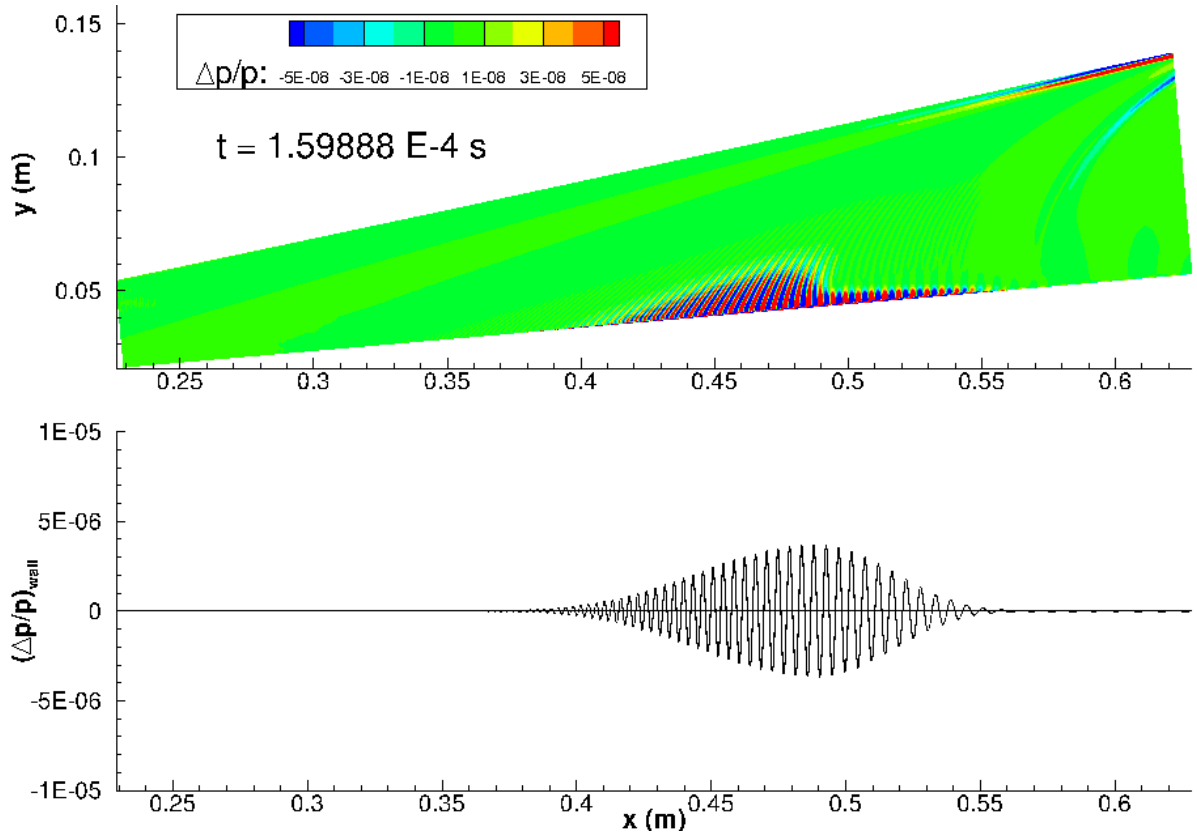
△p/p: -5E-08 -3E-08 -1E-08 1E-08 3E-08 5E-08
t = 1.59888 E-4 s
y (m)
0.15
0.1
0.05
0.25 0.3 0.35 0.4 0.45 0.5 0.55 0.6
1E-05
5E-06
0
-5E-06
-1E-05
(△p/p)wall
x (m)

(c)

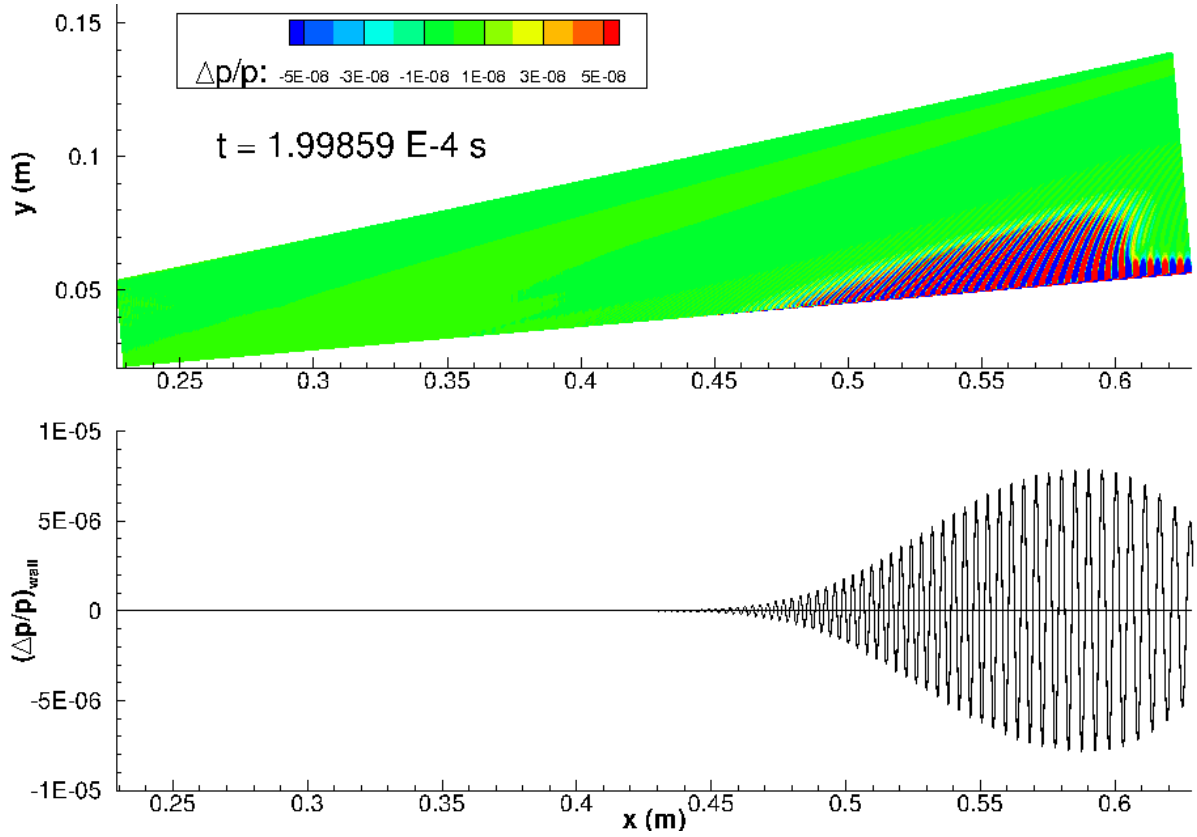
△p/p: -5E-08 -3E-08 -1E-08 1E-08 3E-08 5E-08
t = 1.99859 E-4 s
y (m)
0.15
0.1
0.05
0.25 0.3 0.35 0.4 0.45 0.5 0.55 0.6
1E-05
5E-06
0
-5E-06
-1E-05
(△p/p)wall
x (m)

(d)

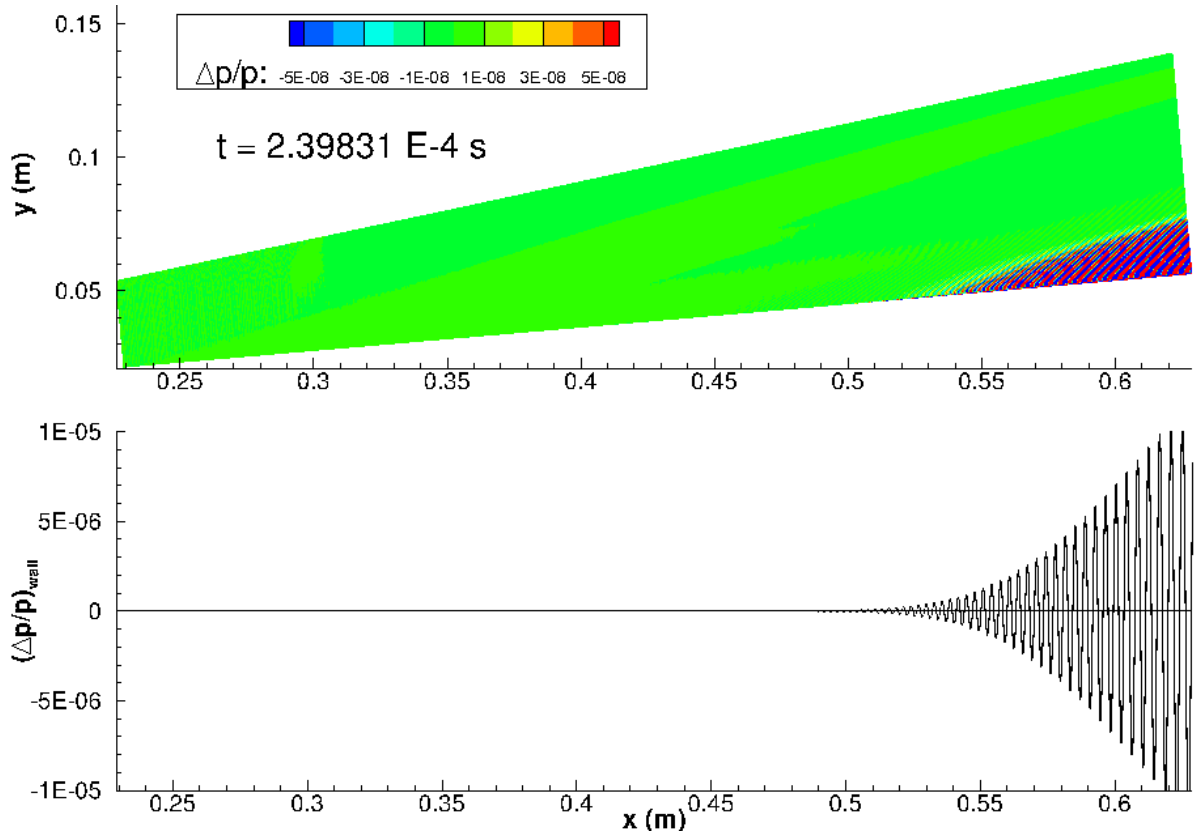

(e)

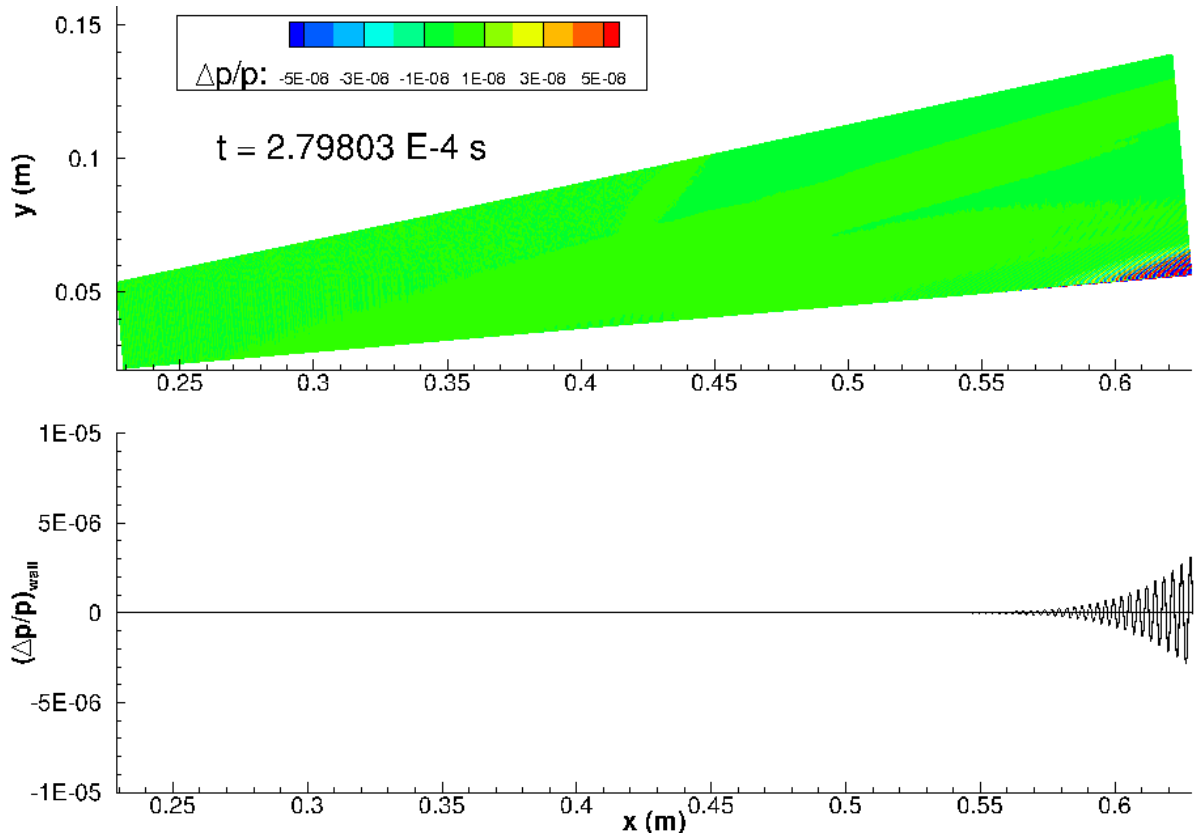

(f)

Figure 16: Snapshots in time of pressure perturbation $\Delta p/p$ contours and surface pressure perturbation from Gaussian pulse. Δt = 3.997 E-5 seconds.

It is worthwhile to compare the results presented in Figure 16 to similar results of a DNS low-frequency wave packets on a flat plate examined by Chuvakhov and Fedorov,[15] where the authors imposed a pulse targeting a single frequency, rather than impose a Gaussian pulse as used here. Chuvakhov and Fedorov's pulse experiences multiple "patches" of radiation from the wall. Here, however, as the disturbance travels downstream, the disturbance travels in a single pulse, rather than breaking up into patches that separate from one another and grow. It is difficult to provide a definitive explanation for the discrepancy between Chuvakhov and Fedorov's results and the results in Figure 16, however it could be due to the Gaussian pulse exciting a continuous range of frequencies as opposed to a band around a single frequency and its harmonics. Additionally, the differing freestream conditions and the nonparallel effects from the conical geometry could play a role.

The unsteady DNS pressure perturbation at time $t = 2.39831E-04$ seconds was compared qualitatively to the LST pressure perturbation at a fixed frequency of $F = 5.65E-04$ ($f = 600$ kHz) evaluated at the same time (Figure 17). The LST perturbation contour has been transformed back into global (x, y) coordinates from the streamwise and wall-normal coordinates for better comparison. The aim of this comparison was to estimate qualitatively which frequencies were contributing the most to the pressure perturbation at an arbitrary location of $x = 0.62m$. While the most unstable frequency at this location is approximately $F = 4.71E-04$ ($f = 500$ kHz), the mode associated with this frequency is not predicted to have synchronized with the slow acoustic spectrum yet. The unstable LST mode associated with $F = 5.65E-04$ ($f = 600$ kHz) was chosen because it is roughly half way between the most unstable frequency and the neutral frequency at this location.

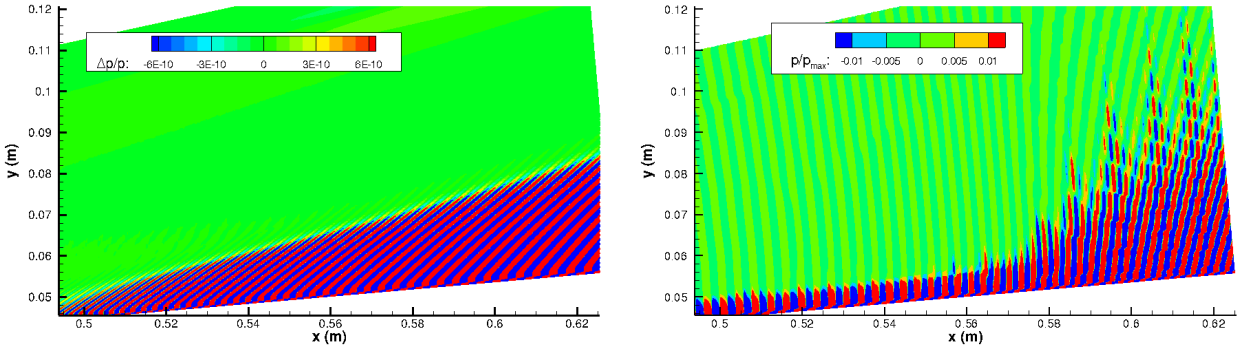

(a) (b)

Figure 17: Qualitative comparison of pressure perturbation contours at $t = 2.39831E-04$ seconds. (a) DNS. (b) LST at $F = 5.65E-04$ ($f = 600$ kHz). LST contours have been locally scaled by their absolute maximum value at each streamwise location. DNS contours have been scaled by the local mean flow values.

The first qualitative comparison made from Figure 17 is that the location in which the spontaneous radiation of sound occurs predicted by the LST contour coincides roughly with the unsteady DNS results. This indicates that the LST reasonably predicts the onset of the supersonic modes. However, one of the shortcomings of LST is that only one frequency is considered at a time, whereas in reality the disturbance is composed of infinitely many frequencies. This drawback is of importance in comparing the wave angle created by the radiation of sound. The wave angle at $x = 0.62$ m from the DNS results is $\theta \approx 42.2$ degrees with respect to the wall, and the wave angle at the same location for the LST results is $\theta \approx 70.8$ degrees. This result indicates that there are other major contributing frequencies to the radiation of sound in the DNS case. As mentioned in the LST results, the wave angle increases clockwise from perpendicular, or in this context, the wave angle with respect to the wall will decrease as the perturbation travels downstream. Because the LST wave angle is greater than the DNS wave angle, this indicates that the frequency $F = 5.65E-04$ ($f = 600$ kHz) is not the major contributor to the spontaneous radiation of sound. For the LST wave angle to be greater at $x = 0.62$ m ($R \approx 1030$), it would mean that the supersonic mode must be created further upstream. Referencing the LST neutral stability map in Figure 8, for a fixed location, this would require the LST frequency to be higher. Therefore, one could conjecture that it is the higher unstable frequencies that contribute the most to the spontaneous radiation of sound. In this particular example, the

major contributing frequencies to the spontaneous radiation of sound may be between the neutral frequency $F \approx 6.0E-04$ ($f \approx 640$ kHz) and the examined frequency $F = 5.65E-04$ ($f = 600$ kHz). Fourier transform (FFT) analyses of the unsteady DNS are required to determine the influence of each frequency on the growth of the disturbance. It is likely that there is no major contributing frequency to the spontaneous radiation of sound; rather, it may be the collective interaction of all of the unstable supersonic modes that causes this phenomenon.

The mode shape of the pressure disturbance was extracted from the unsteady DNS results for both a subsonic and supersonic mode. This wall-normal pressure disturbance profile was then compared to the LST pressure mode shape for a fixed frequency. The DNS pressure disturbance magnitude is normalized by the magnitude of the pressure disturbance at the wall. A subsonic mode at $R = 718$ ($s = 0.300$m) obtained at $t = 0.7994E-4$s is shown in Figure 18(a), and a supersonic mode at $R = 1036$ ($s = 0.624$m) obtained at $t = 2.39831E-04$s is shown in Figure 18(b). At $R = 718$, the dominant frequency predicted by LST is approximately $F = 7.53E-04$ ($f = 800$kHz), and at $R = 1036$, the dominant frequency is approximately $F = 5.18E-04$ ($f = 550$kHz). Because at $R = 1036$ the frequency $F = 5.18E-04$ is not a supersonic mode, the supersonic mode associated with the frequency $F = 5.65E-04$ ($f = 600$kHz) was also included for comparison in Figure 18(b). It appears that the LST mode shape more closely resembles the unsteady DNS pressure perturbation for the subsonic mode than the supersonic mode. This helps reinforce the notion that the supersonic mode is a collection of frequencies interacting to create a complex mode shape that cannot be accurately described by a singular dominant frequency.

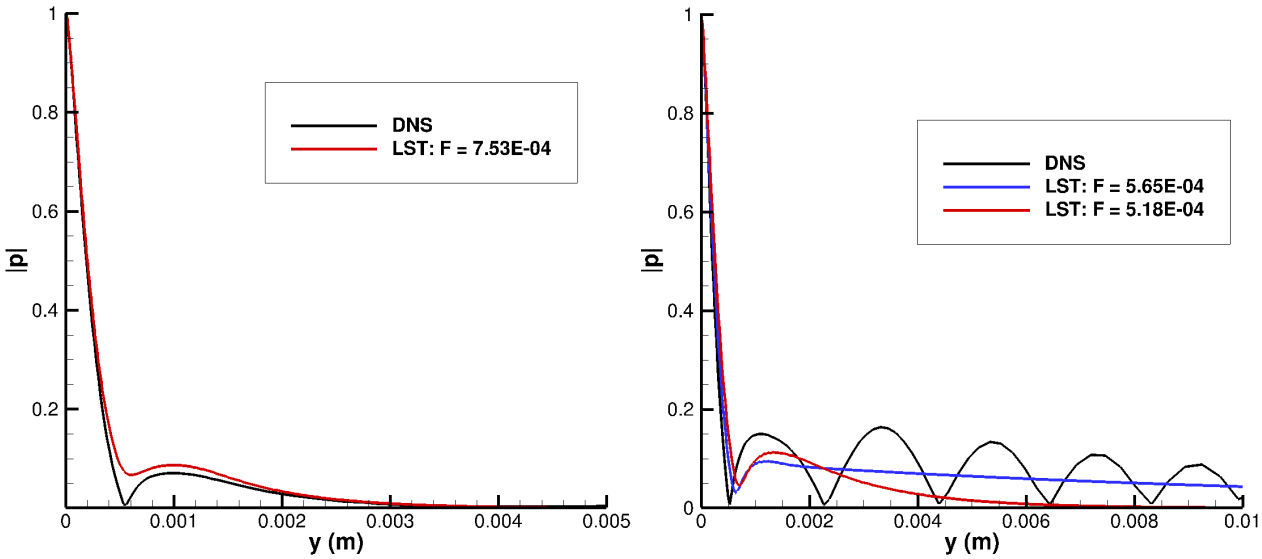

(a) (b)

Figure 18: Comparison of magnitude of DNS wall-normal pressure perturbation normalized by magnitude of pressure perturbation at the wall to LST eigenfunctions. (a) Subsonic mode. $R = 752$ ($s = 0.300$m), $t = 0.7994E-4$s, $F = 7.53E-04$ ($f = 800$kHz). (b) Supersonic mode. $R = 1036$ ($s = 0.624$m), $t = 2.39831E-04$s, $F = 5.18E-04$ and $F = 5.65E-04$ ($f = 550$kHz and $f = 600$kHz).

To quantitatively determine which frequencies were contributing to the second mode growth, the time history of the pulse perturbation on the surface of the cone at each streamwise location was recorded. The pressure perturbation time history for streamwise locations spaced 5cm apart is shown in Figure 19. Presenting the data in this fashion allows for the visualization of the wave fronts in a similar manner as Figure 16, however a Fourier transform of the time history yields the frequency content of the pulse rather than the wavenumber content. From Figure 19, it is clear that the front of the pulse is traveling quicker than the tail-end of the pulse, resulting in the elongation of the disturbance region.

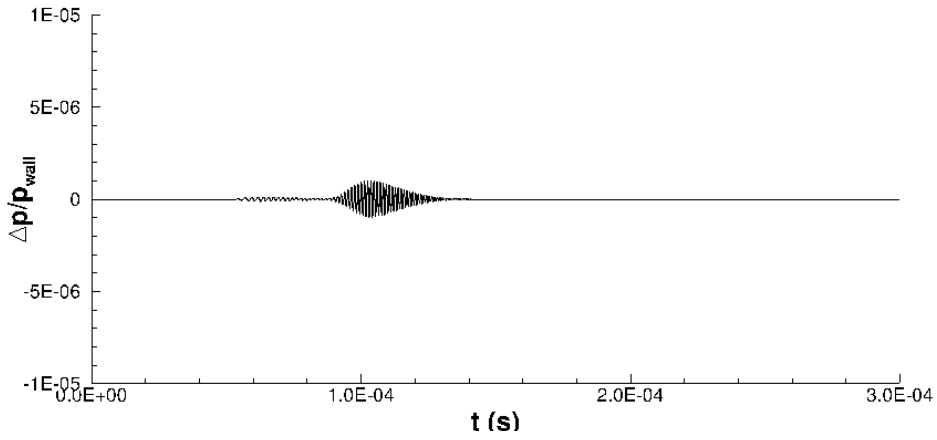
1E-05
5E-06
0
-5E-06
-1E-05
Δp/p_wall
0.0E+00
1.0E-04
2.0E-04
3.0E-04
t (s)

(a)

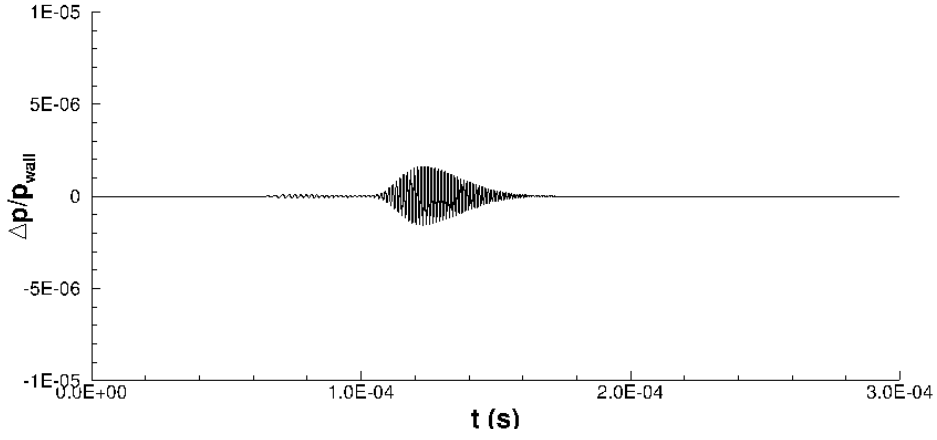
1E-05
5E-06
0
-5E-06
-1E-05
Δp/p_wall
0.0E+00
1.0E-04
2.0E-04
3.0E-04
t (s)

(b)

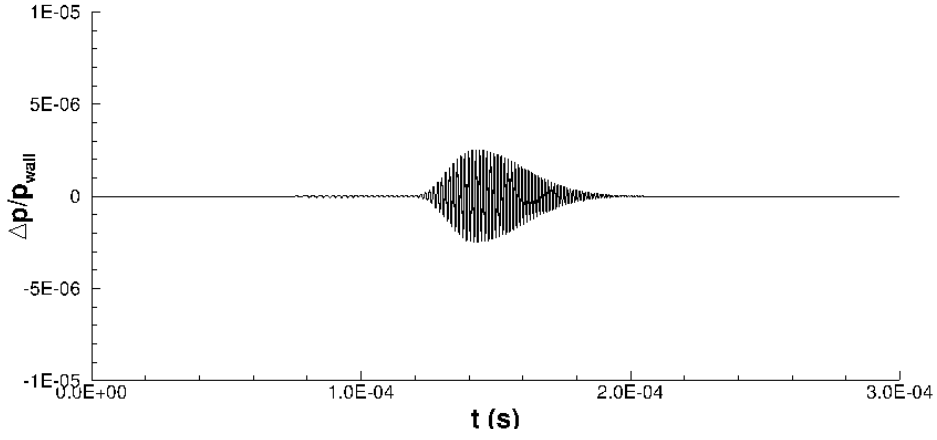
1E-05
5E-06
0
-5E-06
-1E-05
Δp/p_wall
0.0E+00
1.0E-04
2.0E-04
3.0E-04
t (s)

(c)

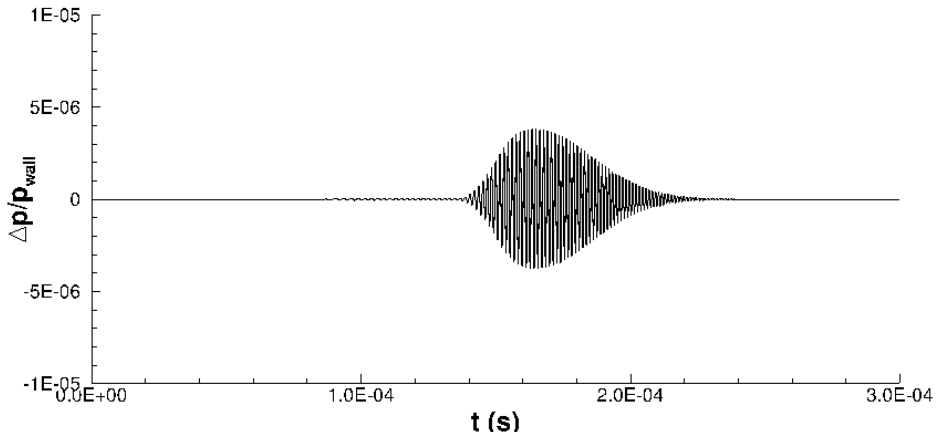

(d)

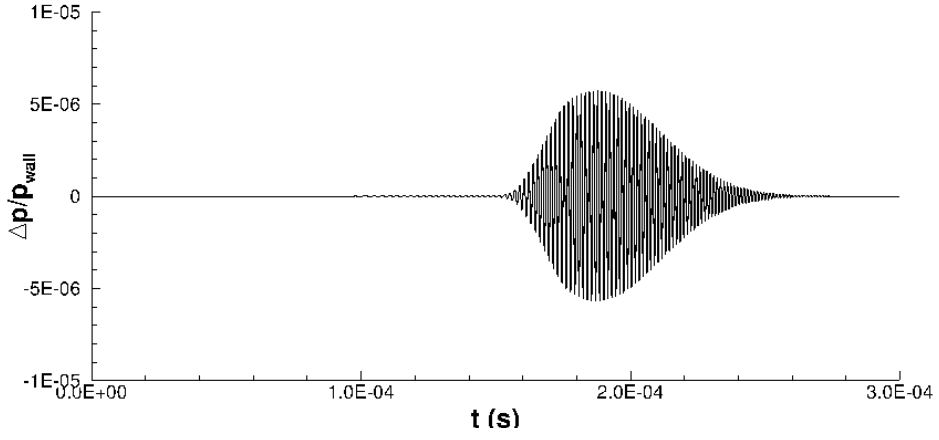

(e)

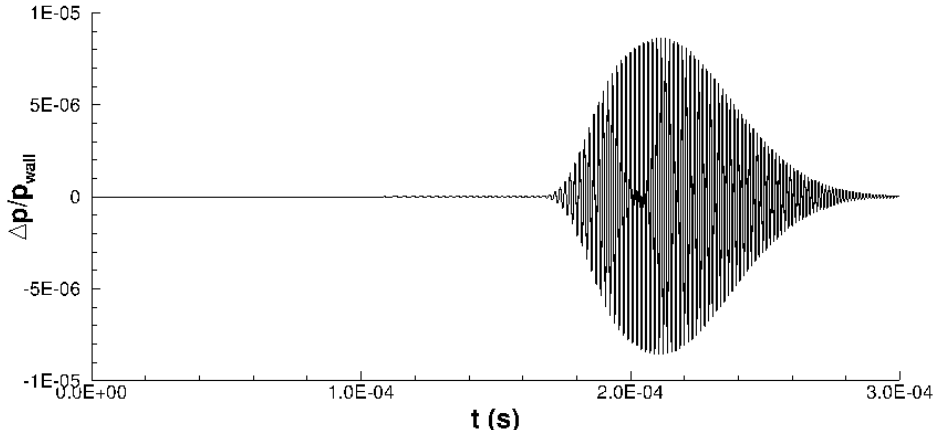

(f)

Figure 19: Time history of surface pressure perturbation from Gaussian pulse at (a) $s = 33.5$cm, (b) $s = 38.5$cm, (c) $s = 43.5$cm, (d) $s = 48.5$cm,(e) $s = 53.5$cm, (f) $s = 58.5$cm. $\Delta x = 5$cm.

A FFT was performed for the surface pressure perturbation at all streamwise locations, resulting in the contour map in Figure 20. This contour shows the most unstable excited frequencies due to the Gaussian pulse. The neutral stability curve predicted by LST from Figure 8 is overlayed in Figure 20 for comparison. It appears that there are a number of frequencies that undergo a significant amplification, however the

most amplified frequency is approximately $f = 625$ kHz and appears most prominently for $s > 0.55$ m. This frequency is near the most unstable frequency predicted by LST, and the location of the maximum amplification agrees reasonably well with the LST predictions.

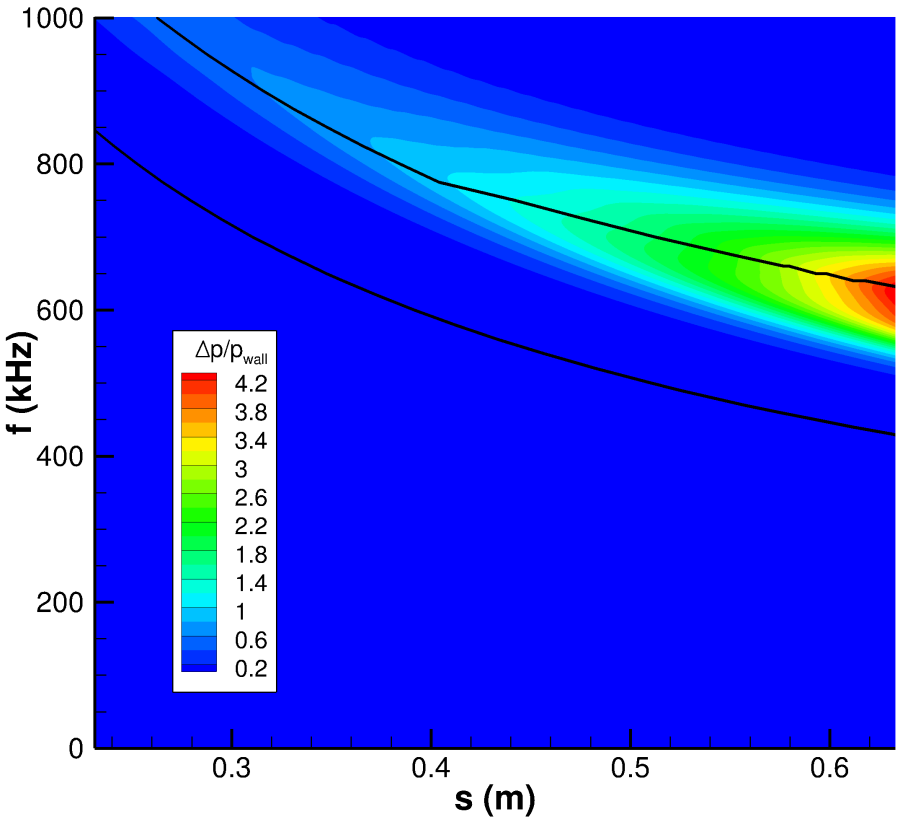

Figure 20: Fourier transform of unsteady surface pressure perturbation time history of Gaussian pulse. The black line is the neutral curve predicted by LST.

Again, it is useful to compare the FFT results to those obtained by Chuvakhov and Fedorov,[15] although their unsteady DNS perturbs the flow with a sinusoidal pulse in time, rather than the Gaussian pulse that is used here. This essentially targets a specific frequency range (with some harmonic frequencies) to excite , rather than the broad range of frequencies excited by the Gaussian pulse. In any case, Chuvakhov and Fedorov[15] are able to take a Fourier transform of the unsteady data and present the FFT of the pressure perturbation vs frequency for fixed streamwise locations. An example of such a figure is shown in Figure 21 for the current investigation, where the curve shape is similar to a bell curve. Chuvakhov and Fedorov[15] again obtained somewhat different results for their study. They noted that rather than the typical bell-shaped curves, multiple peaks are formed. Chuvakhov and Fedorov[15] observed three peaks at most in their FFT, which may have been due to the unsteady pulse only exciting a few frequencies, rather than a broader range of frequencies. Furthermore, the geometry and flow conditions differ significantly from the current study. The same authors have suggested the mechanism of sound radiation acts as an energy sink, which may explain the abnormal behavior of the pulse dispersion. Further detailed investigation into this phenomenon is required to ascertain the mechanism by which the spontaneous radiation of sound modulates the surface pressure perturbation, and whether or not the frequency content of the disturbance plays a significant role in the spontaneous radiation of sound.

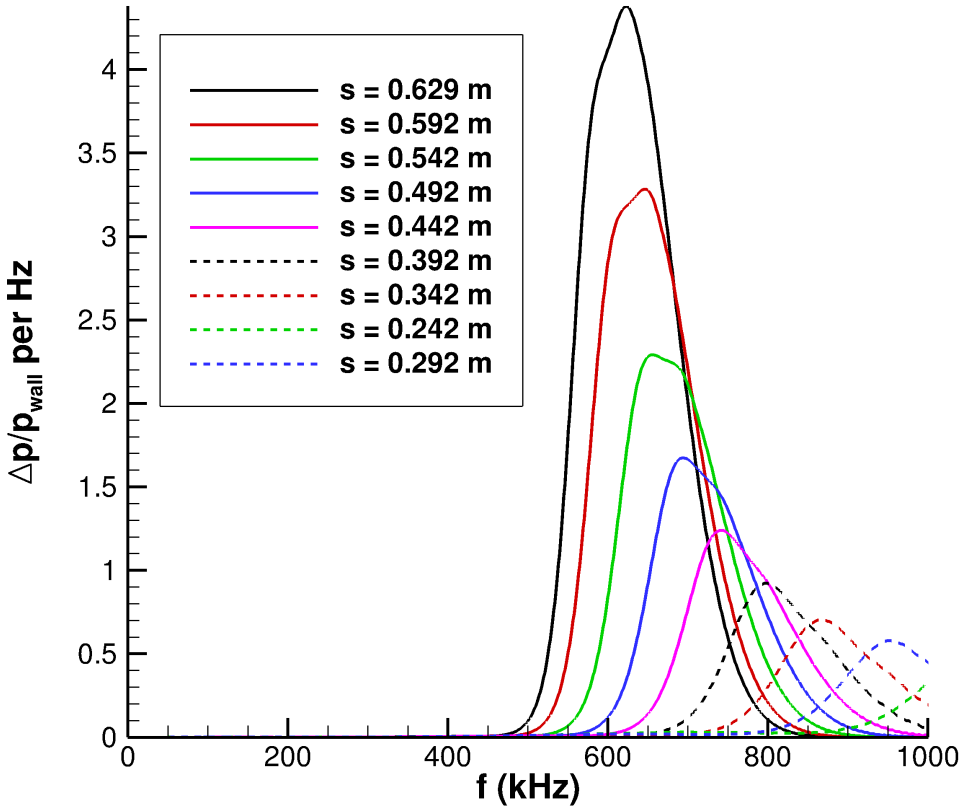

Figure 21: Fourier transform of unsteady surface pressure perturbation time history of Gaussian pulse as a function of frequency for various streamwise locations s.

It is also useful to examine the FFT of the pressure perturbation as a function of streamwise distance for a fixed frequency (Figure 22). This shows the growth of the perturbation from some initial amplitude as the disturbance travels down stream. The single peak seen in the FFT contour are present here as well. For example, $f = 600$ kHz is near the most amplified frequency; therefore the neighboring frequencies $f = 660$ kHz and $f = 560$ kHz are observed to be less amplified. Regardless of the maximum amplitude, all frequencies undergo the exponential-like growth that is characteristic of second mode growth.

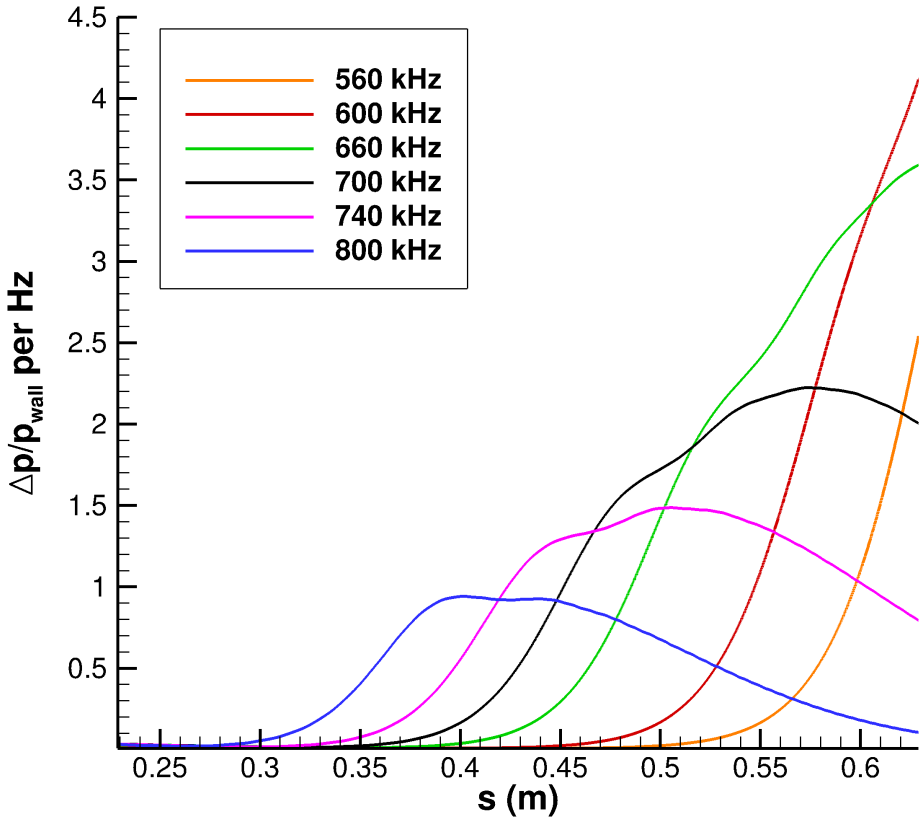

Figure 22: Fourier transform of unsteady surface pressure perturbation time history of Gaussian pulse as a function of streamwise distance for various frequencies.

It is possible to determine the growth rate and phase speed of an unsteady disturbance in DNS. The Fourier decomposed perturbation variables can be used to reconstruct the perturbation original flow field disturbances via

$$\phi'(x,y,t) = \Delta\phi(x,y)\exp\left[i(\psi(x,y) - 2\pi f t)\right] \tag{54}$$

where ϕ' is the perturbation of some variable, $\Delta\phi$ is the amplitude of that variable, ψ is the corresponding phase angle, and f represents a single dimensional frequency. An instantaneous snapshot of the flow field can be obtained from the real part of ϕ' when t is specified, similar to what was done in constructing the 2D LST contours in Equation 52, provided FFT data is available for all data points in the flow field.

Multiple boundary layer modes are present simultaneously in DNS, however as one mode becomes dominant, it is possible to derive growth rate, wave number, and phase speed equations for a given frequency f from Equation 54, resulting in

$$-\alpha_i = \frac{1}{\Delta\phi(f)}\frac{d}{ds}\Delta\phi(f) \tag{55}$$

$$\alpha_r = \frac{d}{ds}\psi(f) \tag{56}$$

$$c_r = \frac{2\pi f}{\alpha_r} \tag{57}$$

$$\tag{58}$$

where s is the streamwise coordinate, $\Delta\phi(f)$ represents a variable amplitude frequency f, and $\psi(f)$ represents the corresponding phase angle at frequency f. Similar to previous researchers,[52] the surface pressure perturbations from DNS are used to compute $-\alpha_i$ and c_r.

As noted from the FFT of the surface pressure perturbation in Figure 20, the frequency $f = 700$ kHz undergoes significant amplification due to the supersonic mode. Therefore, this frequency was chosen to compare the phase speed and growth rate obtained from DNS to those predicted by LST (Figure 23). The phase speed calculated from DNS matches the LST predictions quite well, with the exception of oscillations between $s < 0.4$ m. These oscillations are the result of the synchronization of mode F1 with mode S and with the entropy/vorticity spectra. The DNS growth rate exhibits much more oscillatory behavior, although still follows the LST prediction reasonably well. The DNS growth rate is larger than the LST growth rate because there are contributions from multiple modes. Interestingly, the DNS growth rate also displays the "kink" predicted by the LST near $s = 0.48$ m, which indicates synchronization of the mode F1$^+$ with the slow acoustic spectrum, leading to the spontaneous radiation of sound.

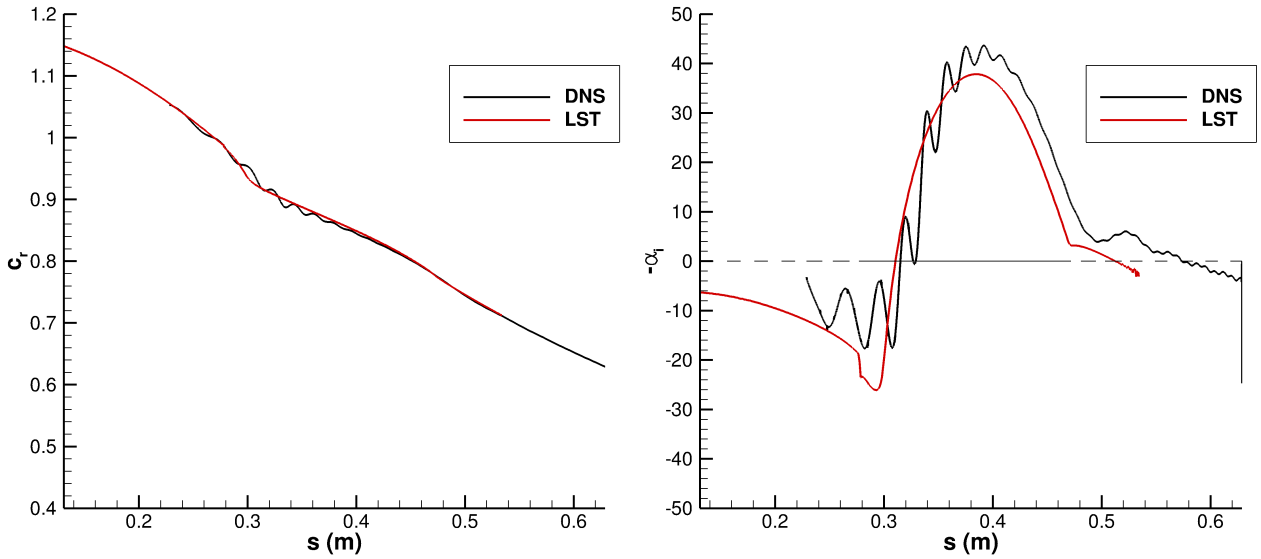

(a) (b)

Figure 23: Comparison of DNS to LST phase speed and growth rate at $f = 700$ kHz. (a) Phase speed, c_r. (b) Growth rate, $-\alpha_i$.

For comparison to the 700 kHz disturbance, the phase speed and growth rate of a weaker frequency $f = 800$ kHz are shown in Figure 24. Overall, the DNS results generally oscillate around the LST predictions, however the agreement at this frequency is not as strong. Because $f = 800$ kHz is not as greatly amplified, the influence of other modes, particularly the acoustic modes, is greater. This is evidenced by the DNS growth rate oscillating for $s > 0.4$ rather than following the LST prediction.

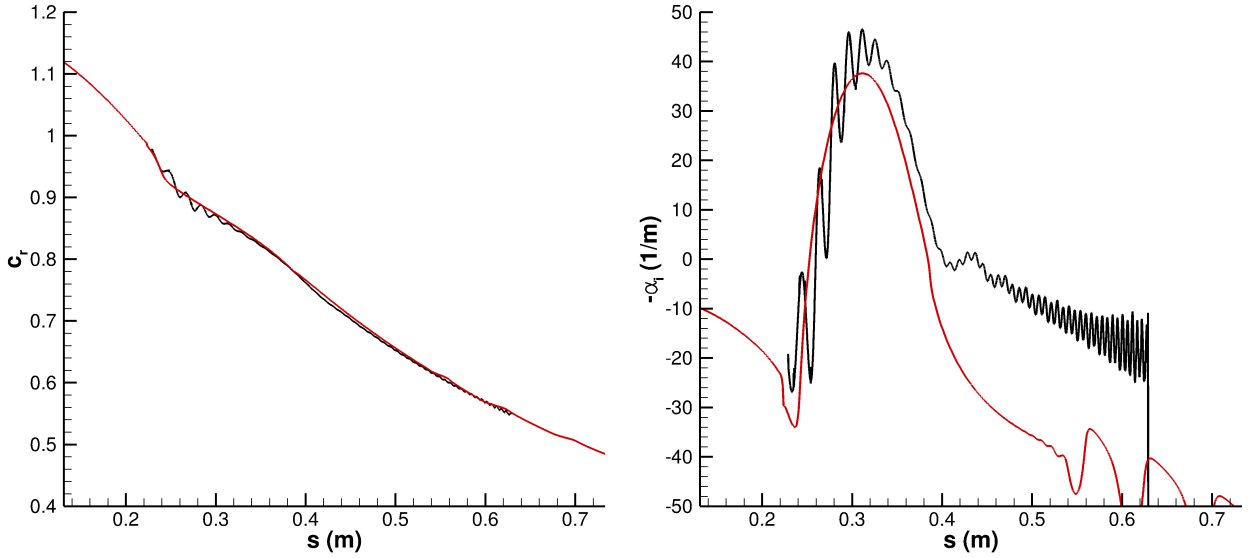

(a) (b)

Figure 24: Comparison of DNS to LST phase speed and growth rate at $f = 800$ kHz. (a) Phase speed, c_r. (b) Growth rate, $-\alpha_i$.

To investigate the frequency content of the sound radiation outside the boundary layer, unsteady time-histories and Fourier transform results are presented for the pressure perturbation at a constant wall-normal index $J = 65$, which corresponds to a region that is in the center of the sound radiation from the wall. For example, at $s = 0.62$, the data is extracted at approximately $y = 0.0035$ m from the wall. The pressure perturbation amplitude at this location is nearly two orders of magnitude smaller than the pressure perturbation at the surface. Despite the smaller amplitude, the overall shape of the disturbance is the same for the perturbation in the middle of the flow as it is for the perturbation at the wall. The time history of the pressure perturbation in the middle of the flow is shown in Figure 25, and the FFT of the time history of the pressure perturbation is shown in Figure 26.

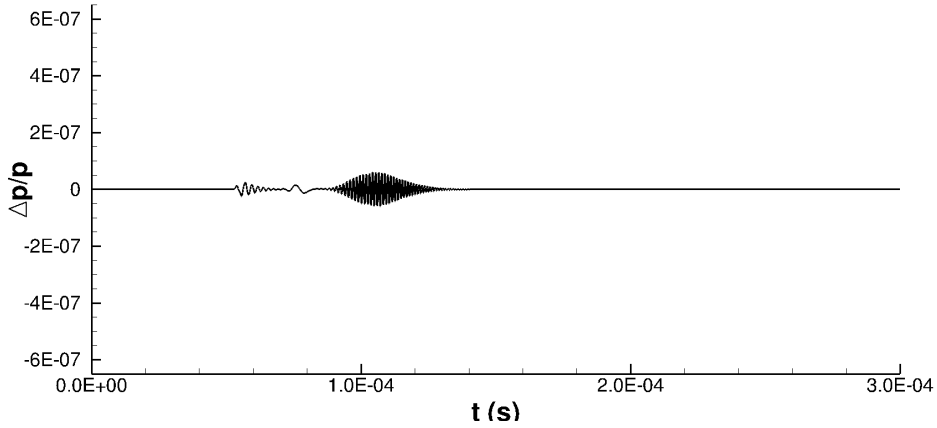
6E-07
4E-07
2E-07
0
-2E-07
-4E-07
-6E-07
Δp/p
0.0E+00
1.0E-04
2.0E-04
3.0E-04
t (s)

(a)

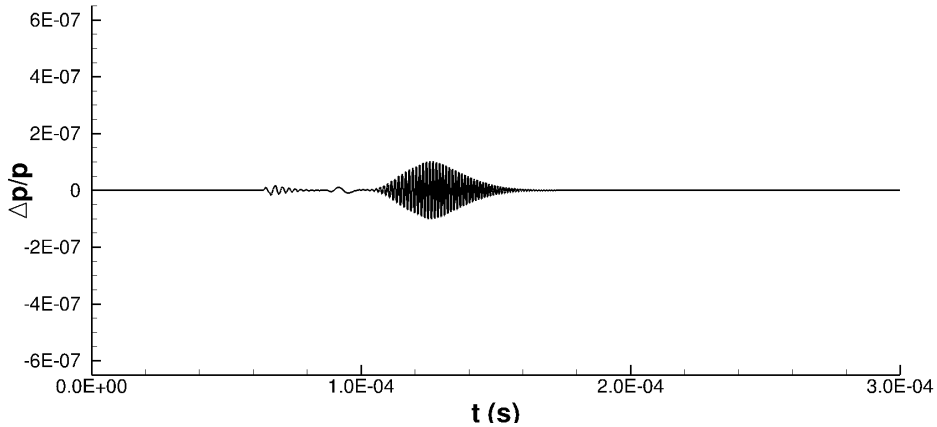
6E-07
4E-07
2E-07
0
-2E-07
-4E-07
-6E-07
Δp/p
0.0E+00
1.0E-04
2.0E-04
3.0E-04
t (s)

(b)

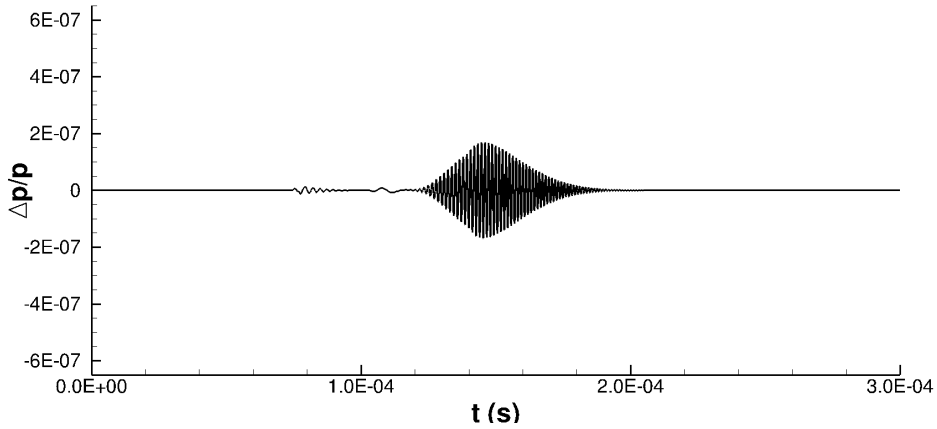
6E-07
4E-07
2E-07
0
-2E-07
-4E-07
-6E-07
Δp/p
0.0E+00
1.0E-04
2.0E-04
3.0E-04
t (s)

(c)

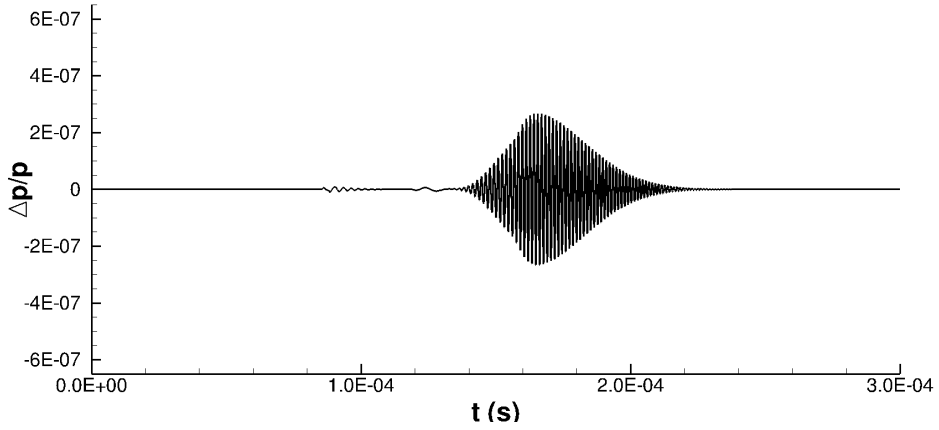

(d)

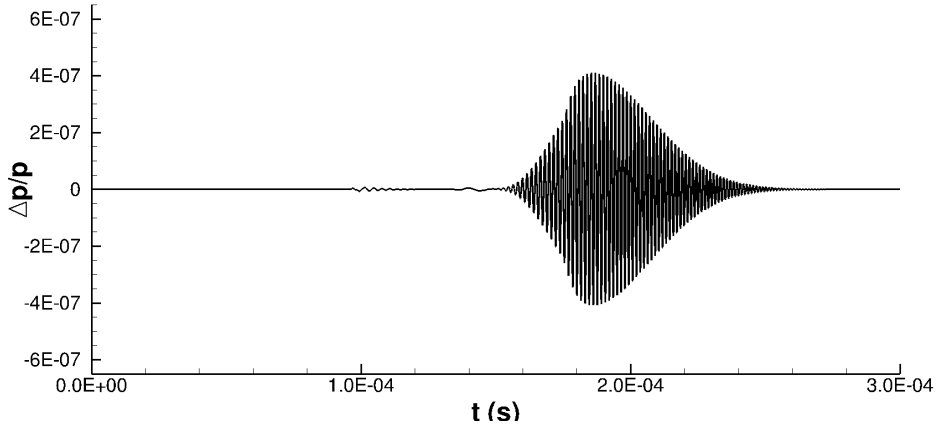

(e)

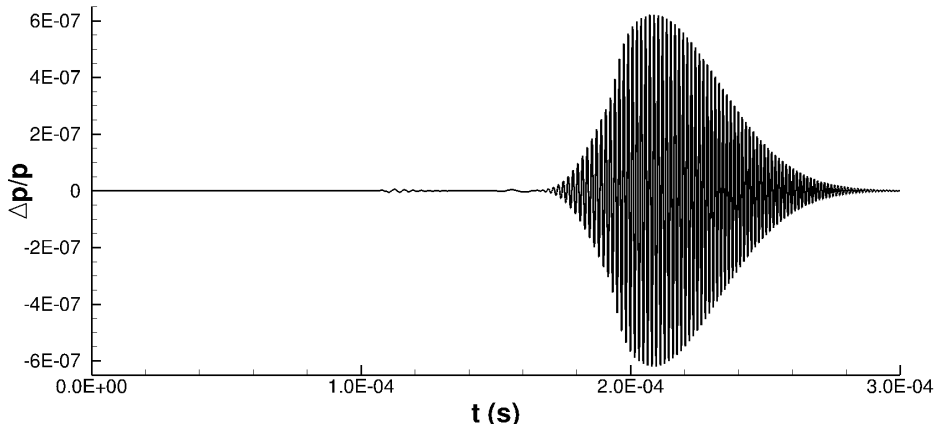

(f)

Figure 25: Time history of pressure perturbation at index $J = 65$ from Gaussian pulse at (a) $s = 33.5$cm, (b) $s = 38.5$cm, (c) $s = 43.5$cm, (d) $s = 48.5$cm,(e) $s = 53.5$cm, (f) $s = 58.5$cm. $\Delta x = 5$cm.

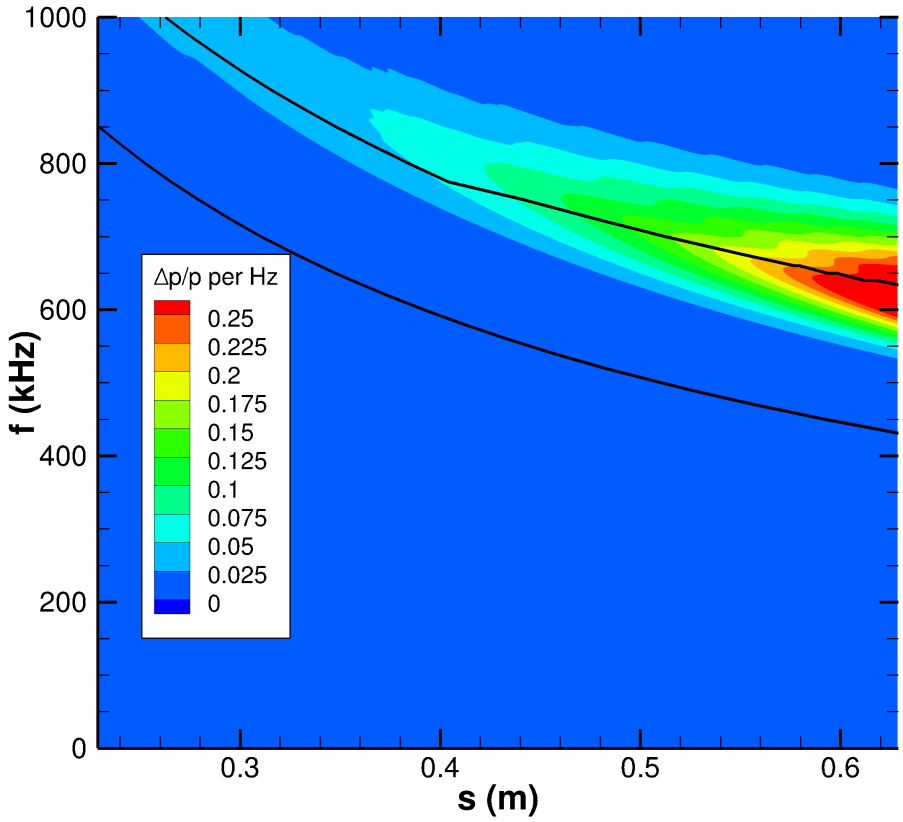

Figure 26: Fourier transform of unsteady pressure perturbation time history at index $J = 65$ of Gaussian pulse. The black line is the neutral curve predicted by LST.

The frequency content of the pressure perturbation outside of the boundary layer at $J = 65$ indicates the most excited frequencies by the Gaussian pulse. Although the magnitude of the disturbance in Figure 26 is about 16 times smaller than in Figure 20, it appears that the same frequencies are excited. The most amplified frequency in the region outside of the boundary layer where the spontaneous radiation of sound occurs is approximately $f = 625$ kHz, which is the same frequency that was most amplified on the wall. This indicates that the surface pressure perturbation may be a reasonable predictor of the frequencies excited outside of the boundary layer. This result is intuitive because the perturbation outside of the boundary layer originates at the wall and radiates outward. One would expect a perturbation due to the most excited frequency at the wall that results in the spontaneous radiation of sound to not be modulated greatly as the disturbance moves away from the wall, and therefore retain the same frequency content as the perturbation at the wall.

The unsteady DNS analysis confirms the predictions made by LST. The excited frequencies in the DNS results agree with the most amplified frequencies from LST. Furthermore, it was shown through FFT analysis that the frequencies that are excited in the spontaneous radiation of sound outside of the boundary layer are nearly identical to the excited frequencies at the wall.

VI. Conclusion and Future Research

The supersonic mode has been shown to exist on an axisymmetric cone with a cold isothermal wall through both LST and unsteady DNS analysis, reinforcing the results obtained for the flat plate geometry by Bitter and Shepherd[9] and Chuvakhov and Fedorov.[15] The formation of the supersonic modes is predicted by LST for an individual frequency as a product of the interaction between the discrete boundary layer mode

F1 and the continuous slow acoustic spectrum. Upon synchronization with the slow acoustic spectrum, mode F1 splits into two simultaneously coexisting modes: the unstable mode $F1^+$ and the stable mode $F1^-$. Mode $F1^+$ gradually joins the slow acoustic spectrum and becomes stable, whereas mode $F1^-$ becomes increasingly stable as streamwise distance increases.

LST analysis has also shown the relative Mach number plays a critical role in the structure of the boundary layer disturbances. Specifically, below $M_r = -1$ the disturbance travels downstream supersonically with respect to the meanflow and is confined by the sonic line. Between $M_r = -1$ and $M_r = 1$, the disturbance travels subsonically with respect to the meanflow, resulting in "rope-like" structures. For supersonic modes, there exists a second sonic line at $M_r = 1$, outside of which the disturbance travels upstream supersonically with respect to the meanflow, resulting in "slanted" wave patterns at an angle $\mu = \arcsin(1/M_r)$.

The unsteady DNS results confirmed the supersonic mode existed at approximately the same location as predicted by LST results. The unstable frequencies predicted by the LST analysis corresponded to the most amplified frequencies the unsteady DNS results. The major finding from the FFT results of the unsteady DNS pressure pulse contradict the multiple peak frequencies observed by Chuvakhov and Fedorov.[15] Rather than certain frequencies being more amplified than their neighboring frequencies, the typical bell-shaped curves were obtained for the pressure perturbation as a function of frequency for a fixed location. The discrepancy in the results may have been due to Chuvakhov and Fedorov's unsteady pulse only exciting a single frequency band, rather than a broader range of frequencies. Furthermore, the geometry and flow conditions differ significantly from the current study. The mechanism by which the acoustic radiation modulates the pressure disturbance is not yet well understood, and further studies are required to fully describe this abnormal behavior and determine the influence of the frequency content of the disturbance on the supersonic mode.

By examining the frequency content of the disturbance outside of the boundary layer, it was determined that the most excited frequencies outside of the boundary layer correspond to the same excited frequencies at the wall. This indicates that the frequency content of the perturbation at the wall is a reasonable predictor for the frequency content of the disturbance outside of the boundary layer.

Overall, it was concluded that the radiation of sound is the physical result of the complex interaction of a number of physical modes, and cannot be easily represented by a single dominant frequency. The interaction of the acoustic waves with the boundary layer disturbance is of significance because it could play a role in energy transfer to the vehicle surface and could have an impact on boundary layer stability. The extent of the influence of the supersonic mode on these parameters is yet to be determined.

In future studies, the impact of the wall temperature and high-enthalpy freestream conditions will be investigated. The flow conditions studied here are not extreme enough to produce significant chemical activity, and thus no conclusion regarding the influence of chemical nonequilibrium can be drawn. Additionally, a "hot wall" ($T_w/T_\infty > 1$) may induce more chemical reactions in the boundary layer, which could alter the stability of the second mode in flows with supersonic modes.

Appendix

The nonzero elements of each complex matrix for the nonequilibrium LST shock boundary conditions are given below, where $\vec{\phi} = [\hat{\rho}_1, \hat{\rho}_2, \ldots, \hat{\rho}_{ns}, \hat{u}, \hat{v}, \hat{w}, \hat{T}, \hat{T}_V]^T$ and δ_{ij} is the Kroenecker delta. The subscripts $i, j = 1, 2, \ldots, ns$, where ns is the number of species in the model. The overbars indicating the steady meanflow components have been dropped for simplicity.

The shock boundary equations are repeated here for clarity:

$$\sum_{j=1}^{ns+5} \hat{B}_{ij}\hat{\phi}_j = 0, \quad i = 1, 2, \ldots, ns+4$$

This represents $ns + 4$ equations for $ns + 5$ independent variables, and therefore an additional equation is required to close the system. The closure equations considered were mixture continuity, y-momentum, and

the right-running characteristic equations. The following simplifying terms are introduced

$$
\begin{aligned}
X_s &= i\alpha\Delta(\rho_s u) - i\omega\Delta(\rho_s), \quad s = 1, 2, \ldots, ns \\
X_{ns+1} &= i\alpha\Delta(\rho u^2 + p) - i\omega\Delta(\rho u) \\
X_{ns+2} &= i\alpha\Delta(\rho uv) - i\omega\Delta(\rho v) \\
X_{ns+3} &= i\beta\Delta p \\
X_{ns+4} &= i\alpha\Delta(u(\rho e + p)) - i\omega\Delta(\rho e) \\
X_{ns+5} &= i\alpha\Delta(u\rho e_v) - i\omega\Delta(\rho e_v)
\end{aligned}
$$

where $\Delta()$ is the jump condition across the shock. For example, $\Delta(\rho u) = (\rho u)_\infty - (\rho u)_{shock}$ where the subscript ∞ denotes upstream of the shock and *shock* denotes immediately downstream of the shock. The nonzero components of $\hat{B}$ are

$$
\begin{aligned}
\hat{B}_{i,j} &= X_{ns+1}\delta_{ij}\left(au - v\right) - X_i\left(a\tfrac{\mathcal{R}}{M_j}T + au^2 - uv\right) \\
\hat{B}_{i,ns+1} &= X_{ns+1}a\rho_i - X_i\left(2a\rho u - \rho v\right) \\
\hat{B}_{i,ns+2} &= -X_{ns+1}\rho_i + X_i\rho u \\
\hat{B}_{i,ns+4} &= -X_i a\tfrac{p}{T} \\
\hat{B}_{ns+1,j} &= X_{ns+1}\left(auv - v^2 + \tfrac{\mathcal{R}}{M_j}T\right) - X_{ns+2}\left(au^2 - uv + a\tfrac{\mathcal{R}}{M_j}T\right) \\
\hat{B}_{ns+1,ns+1} &= X_{ns+1}a\rho v + X_{ns+2}\left(\rho v - 2a\rho u\right) \\
\hat{B}_{ns+1,ns+2} &= X_{ns+1}\left(a\rho u - 2\rho v\right) + X_{ns+2}\rho u \\
\hat{B}_{ns+1,ns+4} &= -X_{ns+1}\tfrac{p}{T} - X_{ns+2}a\tfrac{p}{T} \\
\hat{B}_{ns+2,j} &= X_{ns+3}\left(uv - a\tfrac{\mathcal{R}}{M_j}T - au^2\right) \\
\hat{B}_{ns+2,ns+1} &= X_{ns+3}\left(\rho v - 2a\rho u\right) \\
\hat{B}_{ns+2,ns+2} &= X_{ns+3}\rho u \\
\hat{B}_{ns+2,ns+3} &= a\rho u - \rho v \\
\hat{B}_{ns+2,ns+4} &= -X_{ns+3}a\tfrac{p}{T} \\
\hat{B}_{ns+3,j} &= X_{ns+1}\left(au - v\right)\left[c_{v,j}T + e_{vj} + \tfrac{1}{2}(u^2 + v^2) + h_j^o + \tfrac{\mathcal{R}}{M_j}T\right] - X_{ns+4}\left(a\tfrac{\mathcal{R}}{M_j}T - uv + au^2\right) \\
\hat{B}_{ns+3,ns+1} &= X_{ns+1}\left[\left(au - v\right)\rho u + a\left(\rho e + p\right)\right] + X_{ns+4}\left(\rho v - 2a\rho u\right) \\
\hat{B}_{ns+3,ns+2} &= X_{ns+1}\left[\left(au - v\right)\rho v - \left(\rho e + p\right)\right] + X_{ns+4}\rho u \\
\hat{B}_{ns+3,ns+4} &= X_{ns+1}\left(au - v\right)\left[\rho c_v + \tfrac{p}{T}\right] - X_{ns+4}a\tfrac{p}{T} \\
\hat{B}_{ns+3,ns+5} &= \left(au - v\right)\textstyle\sum_{s=1}^{ns}\rho_s\frac{\partial e_{vs}}{\partial T_V} \\
\hat{B}_{ns+4,j} &= X_{ns+1}\left(au - v\right)e_{vj} - X_{ns+5}\left(a\tfrac{\mathcal{R}}{M_j}T - uv + au^2\right) \\
\hat{B}_{ns+4,ns+1} &= X_{ns+1}a\rho e_v + X_{ns+5}\left(\rho v - 2a\rho u\right) \\
\hat{B}_{ns+4,ns+2} &= -X_{ns+1}\rho e_v + X_{ns+5}\rho u \\
\hat{B}_{ns+4,ns+4} &= -X_{ns+5}a\tfrac{p}{T} \\
\hat{B}_{ns+4,ns+5} &= \left(au - v\right)\textstyle\sum_{s=1}^{ns}\rho_s\frac{\partial e_{vs}}{\partial T_V}
\end{aligned}
$$

Acknowledgments

This research was supported by the U.S. Air Force Office of Scientific Research (AFOSR) through the National Defense Science & Engineering Graduate Fellowship (NDSEG) Program. Primary computational resources were provided by the AFOSR, USAF, under AFOSR Grant #FA9550-15-1-0268, monitored by Dr. Ivett Leyva. Additional computational resources were provided by Extreme Science and Engineering Discovery Environment (XSEDE) provided by Texas Advanced Computing Center (TACC) and San Diego Supercomputer Center (SDSC) under grant number TG-ASC090076, supported in part by the National Science Foundation. This research was also supported by a new Office of Naval Research (ONR) Grant (Grant # TBD). Thanks to Michael Miselis for his calculation of the continuous spectra. The views and

conclusions contained herein are those of the authors and should not be interpreted as necessarily representing the official policies or endorsements, either expressed or implied, of the U.S. Air Force Office of Scientific Research or the U.S. Government.

References

[1]Mack, L. M., "Boundary Layer Linear Stability Theory," Tech. rep., AGARD report No. 709, 1984.

[2]Fedorov, A., "Transition and Stability of High-Speed Boundary Layers," *Annual Review of Fluid Mechanics*, Vol. 43, 2011, pp. 79–95.

[3]Malik, M. R., "Numerical Methods for Hypersonic Boundary Layer Stability," *Journal of Computational Physics*, Vol. 86, 1990, pp. 376–413.

[4]Stuckert, G. and Reed, H., "Linear Disturbances in Hypersonic, Chemically Reacting Shock Layers," *AIAA Journal*, Vol. 32, No. 7, 1994, pp. 1384–1393.

[5]Hudson, M. L., Chokani, N., and Candler, G., "Linear Stability of Hypersonic Flow in Thermochemical Nonequilibrium," *AIAA Journal*, Vol. 35, No. 6, 1997, pp. 958–964.

[6]Johnson, H. B., Seipp, T. G., and Candler, G., "Numerical study of hypersonic reacting boundary layer transition on cones," *Physics of Fluids*, Vol. 10, No. 10, 1998, pp. 2676–2685.

[7]Johnson, H. B. and Candler, G., "Hypersonic Boundary Layer Stability Analysis Using PSE-Chem," *AIAA 2005-5023*, 2005.

[8]Johnson, H. B. and Candler, G., "Analysis of Laminar-Turbulent Transition in Hypersonic Flight Using PSE-Chem," *AIAA 2006-3057*, 2006.

[9]Bitter, N. and Shepherd, J., "Stability of highly cooled hypervelocity boundary layers," *Journal of Fluid Mechanics*, Vol. 778, 2015, pp. 586–620.

[10]Sherman, M. M. and Nakamura, T., "Flight test measurements of boundary-layer transition on a nonablating 22 deg cone," *Journal of Spacecraft and Rockets*, Vol. 7, No. 2, 1970, pp. 137–142.

[11]Malik, M. R., "Hypersonic flight transition data analysis using parabolized stability equations with chemistry effects," *Journal of Spacecraft and Rockets*, Vol. 40, No. 3, 2003, pp. 332–344.

[12]Lees, L., "The Stability of the Laminar Boundary Layer in a Compressible Fluid," Tech. Rep. 876, NACA, 1947.

[13]Mack, L., "Review of Linear Compressible Stability Theory," *Stability of Time Dependent and Spatially Varying Flows*, edited by D. Dwoyer and M. Hussaini, Springer-Verlag, 1985, pp. 164–187.

[14]Mack, L., "Effect of cooling on boundary-layer stability at Mach number 3," *Instabilities and Turbulence in Engineering Flows*, edited by D. Ashpis, T. Gatski, and R. Hirsch, Springer-Verlag, 1993.

[15]Chuvakhov, P. and Fedorov, A., "Spontaneous radiation of sound by instability of a highly cooled hypersonic boundary layer," *8th AIAA Flow Control Conference*, , No. AIAA 2016-4245, 2016.

[16]Demetriades., A., "Hypersonic viscous flow over a slender cone; part iii: Laminar instability and transition." *AIAA 74-535*, 1974.

[17]Zhang, C.-H., Tang, Q., and Lee, C.-B., "Hypersonic boundary-layer transition on a flared cone," *Acta Mechanica Sinica*, Vol. 29, No. 1, 2013, pp. 48–53.

[18]Zhong, X. and Ma, Y., "Boundary-layer receptivity of Mach 7.99 flow over a blunt cone to free-stream acoustic waves," *Journal of Fluid Mechanics*, Vol. 556, 2006, pp. 55–103.

[19]Parsons, N., Zhong, X., Kim, J., and Eldredge, J., "Numerical Study of Hypersonic Receptivity with Thermochemical Non-Equilibrium on a Blunt Cone," *AIAA 2010-4446*, 2010.

[20]Heitmann, D. and Radespiel, R., "Simulation of the interaction of a laser generated shock wave with a hypersonic conical boundary layer," *AIAA 2011-3875*, 2011.

[21]Chang, C.-L., Vinh, H., and Malik, M., "Hypersonic Boundary-Layer Stability with Chemical Reactions using PSE," *28th AIAA Fluid Dynamics Conference, Snowmass Village, CO, U.S.A.*, 1997.

[22]Fedorov, A., Soudakov, V., and Leyva, I., "Stability analysis of high-speed boundary-layer flow with gas injection," *7th AIAA Theoretical Fluid Mechanics Conference*, , No. AIAA 2014-2498, 2014.

[23]Fedorov, A., Bres, G., Inkman, M., and Colonius, T., "Instability of hypersonic boundary layer on a wall with resonating micro-cavities," *49th AIAA Aerospace Sciences Meeting*, , No. AIAA 2011-373, 2011.

[24]Bres, G., Inkman, M., Colonius, T., and Fedorov, A., "Second-mode attenuation and cancellation by porous coatings in a high-speed boundary layer," *Journal of Fluid Mechanics*, Vol. 726, 2013, pp. 312–337.

[25]Wagnild, R., *High Enthalpy Effects on Two Boundary Layer Disturbances in Supersonic and Hypersonic Flow*, Ph.D. thesis, University of Minnesota, 240 Williamson Hall, 231 Pillsbury Drive S.E., Minneapolis, MN 55455, May 2012.

[26]Salemi, L., Fasel, H., Wernz, S., and Marquart, E., "Numerical Investigation of Wave-packets in a Hypersonic High-Enthalpy Boundary-Layer on a 5 Degree Sharp Cone," *7th AIAA Theoretical Fluid Mechanics Conference*, , No. AIAA 2014-2775, 2014.

[27]Salemi, L., Fasel, H., Wernz, S., and Marquart, E., "Numerical Investigation of Nonlinear Wave Packets in a Hypersonic High-Enthalpy Boundary Layer on a 5 Degree Sharp Cone," *45th AIAA Thermophysics Conference*, , No. AIAA 2015-2318, 2015.

[28]Salemi, L. and Fasel, H., "Linearized Navier-Stokes Simulations of the Spatial Stability of a Hypersonic Boundary-Layer on a Flared Cone," *53rd AIAA Aerospace Sciences Meeting*, , No. AIAA 2015-0838, 2015.

[29]Salemi, L., Gross, A., Fasel, H., Wernz, S., and Marquart, E., "Linearized Navier-Stokes Calculations of the Spatial Stability of a Hypersonic Boundary Layer on a 5 °Sharp Cone with High Temperature Effects," *52nd Aerospace Sciences Meeting*, , No. AIAA 2014-0430, 2014.

[30]Tumin, A., Private Communication, 2016.

[31]Mortensen, C. H. and Zhong, X., "High-Order Shock-Fitting Method for Hypersonic Flow with Graphite Ablation and Boundary Layer Stability," *AIAA 2012-3150*, 2012.

[32]Mortensen, C. H. and Zhong, X., "Numerical Simulation of Graphite Ablation Induced Outgassing Effects on Hypersonic Boundary Layer Receptivity over a Cone Frustum," *AIAA 2013-0522*, 2013.

[33]Mortensen, C. H. and Zhong, X., "Real Gas and Surface Ablation Effects on Hypersonic Boundary Layer Instability over a Blunt Cone," *AIAA 2013-2981*, 2013.

[34]Mortensen, C. H. and Zhong, X., "Simulation of Second-Mode Instability in a Real-Gas Hypersonic Flow with Graphite Ablation," *AIAA Journal*, Vol. 52, No. 8, 2014, pp. 1632–1652.

[35]Mortensen, C. H. and Zhong, X., "Numerical Simulation of Hypersonic Boundary-Layer Instability in a Real Gas with Two-Dimensional Surface Roughness," *AIAA 2015-3077*, 2015.

[36]Mortensen, C. H., *Effects of Thermochemical Nonequilibrium on Hypersonic Boundary-Layer Instability in the Presence of Surface Ablation and Isolated Two-Dimensional Roughness*, Ph.D. thesis, University of California Los Angeles, 2015.

[37]Park, C., *Nonequilibrium Hypersonic Aerothermodynamics*, John Wiley & Sons Inc., New York, 1990.

[38]Lee, J., "Basic Governing Equations for the Flight Regimes of Aeroassisted Orbital Transfer Vehicles," *Thermal Design of Aeroassisted Orbital Transfer Vehicles*, edited by H. F. Nelson, Vol. 96, AIAA, 1985, pp. 3–53.

[39]Blottner, F., Johnson, M., and Ellis, M., "Chemically Reacting Gas Viscous Flow Program for Multi-Component Gas Mixtures," Tech. Rep. SC-RR–70-754, Sandia National Laboratories, 1971.

[40]Wilke, C., "A Viscosity Equation for Gas Mixtures," *The Journal of Chemical Physics*, Vol. 18, No. 4, 1950, pp. 517–519.

[41]Zhong, X., "High-Order Finite-Difference Schemes for Numerical Simulation of Hypersonic Boundary-Layer Transition," *Journal of Computational Physics*, Vol. 144, No. 2, 1998, pp. 662–709.

[42]Liu, Y. and Vinokur, M., "Nonequilibrium Flow Computations. I. An Analysis of Numerical Formulations of Conservation Laws," *Journal of Computational Physics*, Vol. 83, No. 2, 1989, pp. 373–397.

[43]Prakash, A., Parsons, N., Wang, X., and Zhong, X., "High-order Shock-fitting Methods for Direct Numerical Simulation of Hypersonic Flow with Chemical and Thermal Nonequilibrium," *Journal of Computational Physics*, Vol. 230, No. 23, 2011, pp. 8474–8507.

[44]Williamson, J., "Low-Storage Runge-Kutta Schemes," *Journal of Computational Physics*, Vol. 35, No. 1, 1980, pp. 48–56.

[45]Malik, M. and Spall, R., "On the stability of compressible flow past axisymmetric bodies," *Journal of Fluid Mechanics*, Vol. 228, 1991, pp. 443–463.

[46]Hudson, M. L., *Linear Stability of Hypersonic Flows in Thermal and Chemical Nonequilibrium*, Ph.D. thesis, North Carolina State University, 1996.

[47]Klentzman, J., Ulker, E., and Tumin, A., "Projection of the solution of the linearized Navier-Stokes equations in reacting high speed boundary layers onto discrete modes," *AIAA 2012-3149*, 2012.

[48]Anderson, E., Bai, Z., Bischof, C., Blackford, S., Demmel, J., garra, J. D., Croz, J. D., Greenbaum, A., Hammarling, S., McKenney, A., and Sorensen., D., *LAPACK Users' Guide*, Society for Industrial and Applied Mathematics, Philadelphia, PA, 3rd ed., 1999.

[49]Stuckert, G., *Linear Stability Theory of Hypersonic, Chemically Reacting Viscous Flows*, Ph.D. thesis, Arizona State University, 1991.

[50]Chang, C.-L., Malik, M., and Hussaini, M., "Effects of shock on the stability of hypersonic boundary layers," *21st AIAA Plasma Dynamics and Lasers Conference*, , No. AIAA 90-1448, 1990.

[51]Mack, L., "Computation of the Stability of the Laminar Compressible Boundary Layer," *Methods in Computational Physics*, edited by B. Alder, S. Fernbach, and M. Rotenberg, Vol. 4, Academic Press, 1965, pp. 247–299.

[52]Ma, Y. and Zhong, X., "Receptivity of a supersonic boundary layer over a flat plate. Part 1. Wave structures and interactions," *Journal of Fluid Mechanics*, Vol. 488, 2003, pp. 31–78.

[53]Fedorov, A. and Tumin, A., "High-speed boundary-layer instability: old terminology and a new framework," *AIAA Journal*, Vol. 49, No. 8, 2011, pp. 1647–1657.

[54]Balakumar, P. and Malik, M. R., "Discrete modes and continuous spectra in supersonic boundary layers," *Journal of Fluid Mechanics*, Vol. 239, 1992, pp. 631–656.

[55]Gaydos, P. and Tumin, A., "Multimode Decomposition in Compressible Boundary Layers," *AIAA Journal*, Vol. 42, No. 6, 2004, pp. 1115–1121.

[56]Tumin, A., "Three-Dimensional Spatial Normal Modes in Compressible Boundary Layers," *AIAA 2006-1109*, 2006.

[57]Tumin, A., "Three-dimensional spatial normal modes in compressible boundary layers," *Journal of Fluid Mechanics*, Vol. 586, 2007, pp. 295–322.

[58]Fedorov, A. and Tumin, A., "Initial-Value Problem for Hypersonic Boundary-Layer Flows," *AIAA Journal*, Vol. 41, No. 3, 2003, pp. 379–389.